Open Research Online

The Open University's repository of research publications
and other research outputs

Callisto's atmosphere: First evidence for H_2 and constraints on H_2O

Journal Item

For guidance on citations see FAQs.

Version: Version of Record

oro.open.ac.uk

Correspondence to:
S. R. Carberry Mogan,
CarberryMogan@berkeley.edu

Callisto's Atmosphere: First Evidence for H_2 and Constraints on H_2O

Shane R. Carberry Mogan[1,2,3,4,5] ![ORCID], Orenthal J. Tucker[6] ![ORCID], Robert E. Johnson[2,7] ![ORCID], Lorenz Roth[5] ![ORCID], Juan Alday[8,9] ![ORCID], Audrey Vorburger[4] ![ORCID], Peter Wurz[4] ![ORCID], Andre Galli[4] ![ORCID], H. Todd Smith[10] ![ORCID], Benoit Marchand[3] ![ORCID], and Apurva V. Oza[4,11] ![ORCID]

[1]Space Sciences Laboratory, University of California, Berkeley, CA, USA, [2]New York University, New York, NY, USA, [3]New York University Abu Dhabi, Abu Dhabi, UAE, [4]University of Bern, Bern, Switzerland, [5]KTH Royal Institute of Technology, Stockholm, Sweden, [6]NASA Goddard Space Flight Center, Greenbelt, MD, USA, [7]University of Virginia, Charlottesville, VA, USA, [8]University of Oxford, Oxford, England, [9]Open University, Milton Keynes, England, [10]Johns Hopkins University Applied Physics Laboratory, Laurel, MD, USA, [11]Jet Propulsion Laboratory, California Institute of Technology, Pasadena, CA, USA

Abstract We explore the parameter space for the contribution to Callisto's H corona observed by the Hubble Space Telescope from sublimated H_2O and radiolytically produced H_2 using the Direct Simulation Monte Carlo method. The spatial morphology of this corona produced via photoelectron and magnetospheric electron-impact-induced dissociation is described by tracking the motion of and simulating collisions between the hot H atoms and thermal molecules including a near-surface O_2 component. Our results indicate that sublimated H_2O produced from the surface ice, whether assumed to be intimately mixed with or distinctly segregated from the dark nonice or ice-poor regolith, cannot explain the observed structure of the H corona. On the other hand, a global H_2 component can reproduce the observation, and is also capable of producing the enhanced electron densities observed at high altitudes by *Galileo*'s plasma-wave instrument, providing the first evidence of H_2 in Callisto's atmosphere. The range of H_2 surface densities explored, under a variety of conditions, that are consistent with these observations is $\sim(0.4$–$1) \times 10^8$ cm^{-3}. The simulated H_2 escape rates and estimated lifetimes suggest that Callisto has a neutral H_2 torus. We also place a rough upper limit on the peak H_2O number density ($\lesssim 10^8$ cm^{-3}), column density ($\lesssim 10^{15}$ cm^{-2}), and sublimation flux ($\lesssim 10^{12}$ cm^{-2} s^{-1}), all of which are 1–2 orders of magnitude less than that assumed in previous models. Finally, we discuss the implications of these results, as well as how they compare to Europa and Ganymede.

Plain Language Summary The surface and atmosphere of Callisto, the outermost Galilean moon of Jupiter, are not well understood. Although water ice is a significant fraction of its bulk composition, there is no consensus on the amount of surface ice nor how that correlates with the amount of atmospheric water vapor produced via sublimation. Similarly, although irradiation of the icy surface by the plasma trapped in Jupiter's magnetic field is expected to release O_2 and H_2 as well as directly eject H_2O into the atmosphere, only near-surface O_2 and trace extended H components have been observed by the Hubble Space Telescope, while H_2O and H_2 have not. By simulating the motion of these four species in Callisto's atmosphere, we estimated the contributions to the extended H atmosphere via dissociation of H_2O and H_2. Using sublimation rates suggested in the literature, H_2O produces too much H near the subsolar point and too little closer to the terminator to reproduce the observation. On the other hand, a more global tenuous H_2 component can explain the Hubble observation, as well as earlier observations made by the *Galileo* spacecraft of a highly extended ionosphere. This provides the first evidence for H_2 in Callisto's atmosphere.

1. Introduction

As the most geologically primitive of the icy Galilean satellites, Callisto has the least well understood atmosphere, limiting our understanding of the evolution of the objects in this important system, soon to be the subject of multiple new spacecraft observations. There is no consensus on the state of water ice on its surface nor how that correlates with the production of atmospheric water vapor. Similarly, although radiolysis is likely the primary source of O_2 in Callisto's atmosphere (Cunningham et al., 2015), the concomitant H_2 component has not yet been identified. Forthcoming exploration of Callisto by ESA's JUpiter ICy moons Explorer (JUICE; e.g., Galli et al., 2022), NASA's Europa Clipper, and CNSA's planned Gan De can help resolve such issues. With

Project Administration: Shane R. Carberry Mogan

Resources: Shane R. Carberry Mogan, Benoit Marchand

Software: Shane R. Carberry Mogan, Orenthal J. Tucker, Juan Alday, Audrey Vorburger, Benoit Marchand

Supervision: Orenthal J. Tucker, Lorenz Roth, Audrey Vorburger, Peter Wurz, Andre Galli, Benoit Marchand

Validation: Shane R. Carberry Mogan, Lorenz Roth, H. Todd Smith

Visualization: Shane R. Carberry Mogan, Audrey Vorburger

Writing – original draft: Shane R. Carberry Mogan, Juan Alday

Writing – review & editing: Shane R. Carberry Mogan, Orenthal J. Tucker, Lorenz Roth, Juan Alday, Audrey Vorburger, Peter Wurz, Andre Galli, H. Todd Smith, Apurva V. Oza

these missions as motivation we expand on our earlier simulations of Callisto's atmosphere (Carberry Mogan et al., 2021b) using the observation of its H corona (Roth et al., 2017a) to examine the limits of both its H_2O and H_2 components.

The importance of the interrelated surface and atmospheric processes at Callisto is exemplified by its O_2 atmosphere (Cunningham et al., 2015) and its H corona (Roth et al., 2017a). The former is likely produced via radiolysis in Callisto's icy surface (e.g., Johnson, 1990) as well as, to a much less extent, via a series of photochemical reactions of sublimated H_2O (e.g., Yung & McElroy, 1977). Since O_2 does not freeze out on the surface, even on the night-side, it permeates the porous regolith and enriches the atmosphere limited primarily by reactions in the regolith and gas-phase ionizing and dissociative processes. An H corona was detected by the Hubble Space Telescope (HST; Roth et al., 2017a), which was suggested to be produced via photolytic or electron-impact dissociation of sublimated H_2O or, possibly, radiolytically produced H_2, with a very small contribution due to direct sputtering from its icy surface. Carberry Mogan et al. (2021b), hereafter referred to as "CM21," showed that even though radiolytically produced H_2 can have a peak-density orders of magnitude less than that of the sublimated H_2O component, it can be the primary producer of H near and beyond the terminator. We follow up on that study by using the morphology of the observed H corona to explore the parameter space of its source to place constraints on the very uncertain amounts of sublimated H_2O and radiolytically produced H_2. Before describing the modeling (Section 2), the results (Section 3), and the implications (Section 4), we first review below the observations of Callisto's atmosphere and ionosphere, of water ice on the surface and its relation to the production of water vapor, as well as the sources and corresponding structure of our proposed H_2 atmospheric component.

The tenuous CO_2 atmosphere observed by *Galileo* (Carlson, 1999) was suggested to be global, and radiolysis was suggested to be one of its possible sources. In addition, *Galileo* radio occultations indicated the presence of a substantial ionosphere located at Callisto's terminator (Kliore et al., 2002). Analogous to the O_2 atmosphere on Europa inferred from oxygen emissions (Hall et al., 1995), the ionosphere was suggested to be sourced by a collisional O_2 atmosphere about 2 orders of magnitude more dense than that of the observed CO_2, $\sim 4 \times 10^8$ cm^{-3}. This substantial, near-surface ionosphere was only seen at western elongation: when the trailing hemisphere (TH) of Callisto was simultaneously illuminated by the Sun and bombarded by the corotating Jovian magnetospheric plasma; i.e., when Callisto's day-side and corotating plasma "ram-side" hemispheres were aligned. On the other hand, a highly extended ionospheric plasma was detected at eastern elongation (Gurnett et al., 1997, 2000): when Callisto's leading hemisphere (LH), which is opposite its ram-side hemisphere, was illuminated. That is, during the C3 and C10 flybys, with a closest approach (C/A) of 1,129 km (1.47R_C, where R_C = 2,410 km is the radius of Callisto; Gurnett et al., 1997) and 535 km (1.22R_C; Gurnett et al., 2000), respectively, as *Galileo* passed through the wake downstream of the corotating Jovian magnetospheric plasma, electron densities orders of magnitude larger than those expected from the background plasma, <1 cm^{-3} (Gurnett et al., 2000), were inferred from its plasma-wave measurements. These electron densities were comparable to those seen near Ganymede (Barth et al., 1997), the source of which was suggested to be an extended neutral component, suggesting a similar feature is also present at Callisto. During the C22 flyby, in which *Galileo* passed by the night-side through the plasma wake at western elongation with a C/A of 2,299 km (1.95R_C) an enhanced extended plasma was not observed (Gurnett et al., 2000), although this was the orbit during which one of the largest electron densities, $\sim (0.8–1.5) \times 10^4$ cm^{-3}, were detected by Kliore et al. (2002) near Callisto's surface, $\sim 8–28$ km.

Observations by the HST-Space Telescope Imaging Spectrograph (STIS) were initially unable to detect ultraviolet (UV) auroral emissions caused by magnetospheric electron-impact ionization of Callisto's atmosphere (Strobel et al., 2002). The authors suggested a possible explanation for this: the Jovian magnetospheric plasma is largely diverted by Callisto's ionosphere. As a result, penetration of magnetospheric electrons into Callisto's atmosphere could not be the source of its near-surface ionosphere. Subsequent atomic oxygen emissions were detected using the HST-Cosmic Origins Spectrograph, which were suggested to be induced by photoelectron impacts in a near-surface, O_2-dominated atmosphere when Callisto's LH was illuminated (Cunningham et al., 2015). The derived O_2 column density, $\sim 4 \times 10^{15}$ cm^{-2}, is an order of magnitude less than that inferred by Kliore et al. (2002) when Callisto's TH was illuminated, $\sim 4 \times 10^{16}$ cm^{-2}. Finally, the HST/STIS observations made by Strobel et al. (2002) were recently revisited and faint emissions above Callisto's limb were detected (Roth et al., 2017a), likely originating from resonant scattering by an H corona.

Even after several decades of research and multiple spacecraft missions, the state of surface water ice at Callisto and the concomitant production of atmospheric water vapor are not well constrained. *Galileo* measurements

of Callisto's gravity field suggest 40% of its bulk composition is ice (Anderson et al., 1997), with later analyses yielding mass fractions of 49%–55% ice (Kuskov & Kronrod, 2005; Spohn & Schubert, 2003). However, estimates for surficial coverage of ice on its LH and TH range from only 5% to 30% (Clark & McCord, 1980; Mandeville et al., 1980; McCord et al., 1998; Pilcher et al., 1972; Roush et al., 1990; Spencer, 1987a) with an additional 0%–10% bound water (Clark & McCord, 1980), while the remainder is a relatively dark silicate and/or carbonaceous material (McCord et al., 1998). Whereas these ranges only refer to the visible ice patches on its surface, others have suggested that ice intimately mixed with the nonice surface material (i.e., "dirty ice") is more abundant with weight fractions ranging from 20 to 90 wt% (Calvin & Clark, 1991; Clark, 1980; McCord et al., 1998; Roush et al., 1990) with an additional 0–10 wt% bound water (Clark, 1980), although much lower weight fractions have also been suggested (e.g., ∼4–6 wt% Spencer, 1987a, 1987b). See CM21 for a more in-depth review of the water ice-related observations and models at Callisto.

Thus, it seems that dark material containing adsorbed H_2O and relatively sparse ice patches are both present to some extent on Callisto's surface. However, until this study, relevant to modeling Callisto's atmosphere only the former has been considered in which the ice and nonice or ice-poor material are intimately mixed and H_2O sublimates at Callisto's warm day-side temperatures producing a locally relatively dense atmospheric component (e.g., Hartkorn et al., 2017; Liang et al., 2005; Vorburger et al., 2015, CM21). On the other hand, when these materials are segregated from each other (e.g., Spencer, 1987b), the areal coverage and local temperatures of the ice patches will primarily determine the net H_2O sublimation rate.

Although gas-phase H_2O has not been detected, the recent Hubble observation of an H corona at Callisto (Roth et al., 2017a) presents a way forward. Analogous to models of Ganymede's atmosphere (Marconi, 2007), Roth et al. (2017a) suggested dissociation of H_2O is the main source for the H on the day-side with a possible contribution from H_2 near the terminator. The H corona was initially thought to be larger at eastern elongation than at western elongation due to the temperature differences of the LH and TH (Roth et al., 2017a). However, the weaker signal from the H corona at western elongation was later found to be affected by absorption in the geocorona (Alday et al., 2017). Because of this issue, herein we solely focus on the H observed at eastern elongation, which was negligibly affected.

Using forward models with and without an H corona, the eastern elongation data were in good agreement with a globally symmetric neutral H component (Roth et al., 2017a, Figure 4 therein), which produces a peak line-of-sight (LOS) column density at the terminator. CM21 showed that even if the H_2O sublimates at the warm day-side surface temperatures, its production of H near the terminator region is negligible and completely dominated by photodissociation of H_2. Indeed this is the case near and beyond Callisto's limb even when the peak density of H_2 is orders of magnitude less dense than that of H_2O (CM21, Figure 5 therein) because of its global extent and relatively large scale height. This spatial distribution of the H corona at eastern elongation will be used below to help constrain both the H_2O and H_2 content of Callisto's atmosphere.

In addition to the above uncertainties for water ice on the surface and its relation to the production of water vapor, estimating the radiolytic source rate for H_2 at Callisto is extremely difficult due to the lack of observational constraints and the uncertainty of the surface composition as well as its exposure to the local plasma environment (e.g., Galli et al., 2022 and references therein). This uncertainty is exacerbated as H_2 can be radiolytically produced from hydrated sulfur (Cartwright et al., 2020) and hydrocarbons (McCord et al., 1997, 1998) in Callisto's nonice or ice-poor material in addition to being produced from the ice, including from any carbonic acid therein (e.g., Johnson et al., 2004). Moreover, the very energetic particles can penetrate the nonice or ice-poor regolith overlying the more ice-rich surface, thereby producing H_2 in the ice, which in turn can diffuse through this lag deposit that insulates the underlying ice inhibiting sublimation. Finally, H_2 is also a *direct* dissociation product of water ice (e.g., Teolis et al., 2017) and vapor (e.g., Huebner & Mukherjee, 2015; Itikawa & Mason, 2005) and can be formed following proton implantation in the surface (e.g., Tucker et al., 2019, 2021).

H_2 has a large scale height (∼250–550 km at Callisto's surface temperatures, ∼80–167 K); and its escape fraction is small (e.g., Carberry Mogan et al., 2020, hereafter referred to as "CM20," CM21), as are the photo-impact and electron-impact destruction rates (Table B1 in Appendix B), so that most H_2 produced returns to the surface. Since these returning molecules do not adsorb efficiently (e.g., Acharyya, 2014; Sandford & Allamandola, 1993), they will permeate the porous regolith, in which reaction rates are also negligible allowing it to thermally desorb back into the atmosphere, where it accumulates. In this way, even a relatively small H_2 source rate can produce a steady-state, collisional atmospheric component (e.g., CM20, CM21).

In 1D models, CM20 assumed the H_2 surface density was related stoichiometrically to the observed O_2, whereas Liang et al. (2005) assumed H_2 was solely produced by dissociative recombination of H_2O^+ and is thus strongly correlated with the sublimated water vapor (Figure 2 therein). However, to explain the spatial profile of the H corona, a 2D model is required. Such a model of Callisto's atmosphere containing H_2O and O_2, as well as a range of thermally desorbed H_2 assumed to be produced by the mechanisms discussed above was implemented in CM21. Below, that work is extended to account for the fate of the H produced from H_2O and H_2. Given the limited information about Callisto's atmosphere and surface, accounting for the spatial distribution of the H corona is shown to help constrain the surface source rates of H_2O and H_2, as well as demonstrate the influence of collisions.

2. Numerical Method

2.1. The Direct Simulation Monte Carlo Method

The Direct Simulation Monte Carlo (DSMC) method (Bird, 1994) simulates macroscopic gas dynamics via molecular kinetics. By implicitly solving the Boltzmann equation, it can be used to model dense fluids, rarefied gasses, and the *transition* from the former to the latter. Thus, it is ideally suited to simulate Callisto's atmosphere as it transitions from thermal equilibrium near the surface to the nonequilibrium rarefied regime (e.g., the exosphere). We have successfully applied the DSMC method to Callisto's atmosphere in earlier studies (CM20, CM21, Carberry Mogan et al., 2021a). Here, it is used to simulate Callisto's atmosphere composed of sublimated H_2O, radiolytically produced H_2 and O_2 components, and H produced from H_2O and H_2 via interactions with photons and magnetospheric electrons in a 2D axisymmetric spherical domain.

The DSMC method simulates stochastic microscopic processes via computational particles, each of which represents a large number of real atoms or molecules. As these particles traverse physical space they are influenced by gravitational forces, binary collisions, and interactions with photons and magnetospheric electrons, and their motion is tracked using a fourth-order Runge Kutta integration. The 2D spherical grid in which these particles move is decomposed into cells that vary along radial and subsolar latitudinal (SSL) axes (Figure A1 in Appendix A).

Elastic collisions between thermal particles are calculated using the variable hard sphere (VHS) model (Bird, 1994) using the parameters listed in CM21 (Appendix D therein). Collisions between hot H atoms and thermal species are calculated using the model in Lewkow and Kharchenko (2014). When calculating collisions between particles representing a different number of atoms or molecules we implement the technique described by Miller and Combi (1994).

A DSMC simulation is temporally discretized into time steps, Δt. Nascent H particles will initially move at velocities relative to the excess energy of the reaction that produces them (Table B1 in Appendix B), and these are much faster than the typical speeds of the thermal species. Therefore, we implement subtime steps, Δt_{sub}, for the H particles. That is, H particles will move $\Delta t / \Delta t_{sub}$ times before the thermal species then move over Δt. Moreover, collision-based calculations between H and the thermal species will occur over each Δt_{sub}, while such calculations between thermal species only occur over Δt.

The DSMC simulations presented herein are run for a long enough duration, on the order of Callisto's orbital period, $t_{orb} = 1.44 \times 10^6$ s, such that the distribution of particles and their corresponding characteristics yield steady-state macroscopic properties, such as density, temperature, and escape rates. Steady-state is determined through periodic sampling and averaging of the flow field. Upon reaching steady-state, the simulations are run for several more t_{orb} with more samples taken to reduce the statistical noise inherent in the results, see Figure F1 in Appendix F.

2.2. Surface Temperature

The relatively warm surface temperatures observed by *Voyager* 1 and 2 (Hanel et al., 1979; Spencer, 1987c) and by *Galileo* (Moore et al., 2004) displayed in Figure 1 are consistent with Callisto's predominantly dark surface. If, however, this warm, dark material were ice-enriched (e.g., Clark, 1980), then a substantial amount of H_2O would sublimate and preferentially migrate away from the equatorial regions and deposit onto midlatitude to high-latitude regions in a relatively short amount of time (e.g., Sieveka & Johnson, 1982; Spencer, 1987b). However, there is no visual evidence for a poleward migration of ice and concomitant polar ice caps (Spencer, 1987b; Spencer &
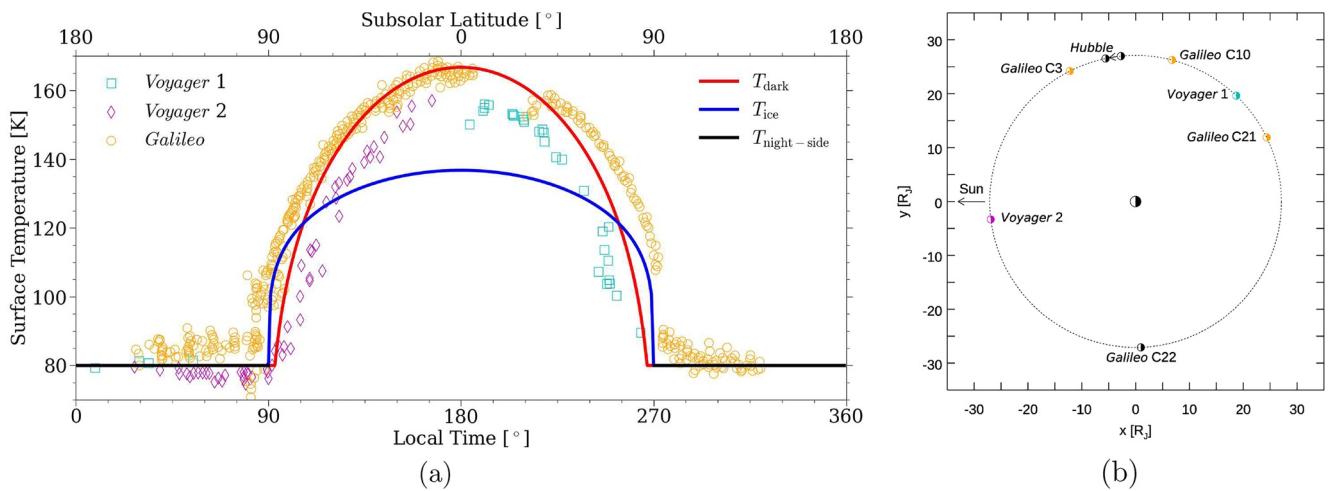
Figure 1. (a) Effective surface temperatures as a function of local time measured by *Voyager* 1 and 2 (Hanel et al., 1979, Figure 7 therein; Spencer, 1987c, Figure 17 therein) and *Galileo* (Moore et al., 2004, Figure 17.7 therein) are plotted as cyan squares, magenta diamonds, and orange circles, respectively. Note the *Galileo* measurements comprise the C3, C10, and C21 encounters. During the *Voyager* 1 and 2 flybys, Callisto's distance from the Sun was 5.29 AU and 5.33 AU, respectively; and the *Galileo* measurements are adjusted to a heliocentric distance of 5.2 AU (Moore et al., 2004). Also plotted are the surface temperature distributions used in this study as a function of subsolar latitude (SSL) for T_{dark} and T_{ice} in red and blue on the day-side (SSL < 90°), respectively, as well as the assumed constant night-side temperature, $T_{night-side}$, in black. Whereas $T_{dark}(SSL)$ is calculated assuming radiative equilibrium with Callisto being 5.2 AU from the Sun (Equation 1), $T_{ice}(SSL)$ is calculated according to the disk-averaged H_2O ice temperature of 115 K derived by Grundy et al. (1999) (Equations 2 and 3). (b) The orbital configurations of Callisto during the aforementioned *Voyager* and *Galileo* flybys in Jupiter radii, $R_J = 71,492$ km. The empty and shaded halves of the circles representing Callisto and Jupiter represent the illuminated and night-side hemispheres, respectively, with the same colors as the corresponding data points from (a). The dotted line represents Callisto's orbit about Jupiter. We also include the C22 flyby for reference to results discussed in Section 4.3 as well as two points representing the start and stop time for the original Hubble observation near eastern elongation in which the H corona was later detected (Strobel et al., 2002).

Maloney, 1984), suggesting that Callisto has a relatively stable surface, dominated by dark nonice or ice-poor material with relatively sparse bright, ice patches from which the sublimation rates are low (Sieveka & Johnson, 1982; Spencer, 1987b; Spencer & Maloney, 1984; Squyres, 1980).

Using the temperature dependence of the near infrared water ice reflectance spectrum, Grundy et al. (1999) derived much colder disk-averaged H_2O ice temperatures at Callisto of $T_{ice} \sim 115 \pm 20$ K. These temperatures are indicative of the sparse, bright ice patches, which are segregated from the dark nonice or ice-poor material (e.g., Spencer, 1987b). Moreover, heat conduction between the higher thermal inertia, bright material and the lower thermal inertia, dark material would be negligible such that the two temperatures remain independent of one another. The proposition of segregated patches of ice and nonice or ice-poor material has been applied to explain images of Callisto's surface (Spencer, 1987b; Spencer & Maloney, 1984) as well as geological processes (Moore et al., 1999). In all previous modeling studies of Callisto's atmosphere, however, only the notion of an intimate mixture of ice and nonice has been considered in which the ice sublimates at Callisto's warm day-side temperatures producing a locally relatively dense atmospheric component (e.g., Hartkorn et al., 2017; Liang et al., 2005; Vorburger et al., 2015, CM21). Hence, prior to this study, the correlation of Callisto's surface temperatures to water production via sublimation has not been extensively explored. Therefore, as described below, we consider two significantly different versions of H_2O production:

1. "Intimate mixture," hereafter referred to as "IM": the ice and dark nonice or ice-poor material are intimately mixed (e.g., Calvin & Clark, 1991; Clark, 1980; Roush et al., 1990), and H_2O sublimates at Callisto's relatively warm day-side temperatures (e.g., Hartkorn et al., 2017; Liang et al., 2005; Vorburger et al., 2015, CM21), T_{dark} (solid red line in Figure 1); and

2. "Segregated patches," hereafter referred to as "SP": the bright ice and dark nonice or ice-poor material are segregated into patches (e.g., Spencer, 1987b), so that H_2O solely sublimates from the former at Callisto's day-side ice temperatures (Grundy et al., 1999), T_{ice} (solid blue line in Figure 1), and the latter sufficiently inhibits sublimation from any underlying ice.
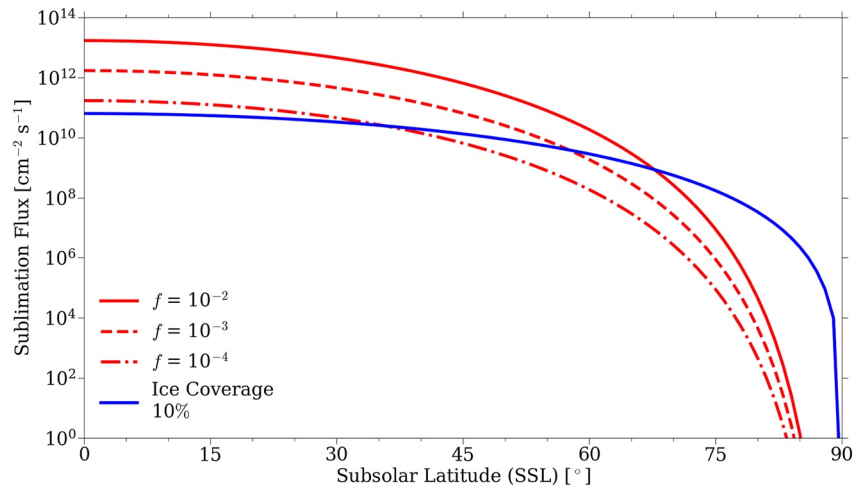
Figure 2. Sublimation fluxes across Callisto's surface for the intimate mixture (IM; red lines) and segregated patches (SP; blue line) scenarios. The solid, dashed, and dash-dotted red lines represent sublimation fluxes for the IM scenario with a sublimation reduction factor of 10^{-2}, 10^{-3}, and 10^{-4}, respectively; and the solid blue line represents the sublimation flux for the SP scenario with an assumed surficial ice coverage of 10%.

2.2.1. Intimate Mixture

Assuming the ice and dark nonice or ice-poor material is intimately mixed, we calculate the day-side surface temperature distribution, T_{dark} (red line in Figure 1), assuming radiative equilibrium with Callisto being 5.2 AU from the Sun, the average distance of the Jovian system from the Sun, which was the case during the original observation of Callisto's atmosphere from which the H corona was later detected (Strobel et al., 2002, Table 1 therein). Spencer (1987c) showed that among the icy Galilean satellites this assumption at Callisto's surface aligned best with the observed surface temperature profiles (Figure 26 therein); and because of its relatively long day and low thermal inertia, midday temperatures observed by *Voyager* are only about 5 K below equilibrium value (magenta diamonds and cyan squares versus red line in Figure 1). T_{dark} is calculated on the day-side (SSL < 90°) using the radiative equilibrium equation

$$\varepsilon \sigma T_{dark}^4 (SSL) = (1 - A) F \cos(SSL) \tag{1}$$

Table 1
Atmospheric Components Simulated and Their Assumed Sources

Component (a)	Source
H_2O	Sublimation with the ice and nonice or ice-poor material either intimately mixed (b) or segregated into patches (b).
H_2	Steady-state thermal desorption of radiolytic product accumulated in the regolith (c) with a uniform surface density ranging from $\sim(0.4–1)\times10^8$ cm^{-3} (d).
O_2	Steady-state thermal desorption of radiolytic product accumulated in the regolith (c) with a uniform surface density of $\sim10^9$ cm^{-3}.
H	Dissociation of H_2O (e) and H_2 (f) molecules via interactions with photons (g) and magnetospheric electrons (g).

[a]Here, we simulate H_2O + H (Figures 3, 4, and 8), H_2 + H (Figures 5–8), H_2O + H_2 + H (Figures 3, 4, and 9), and H_2O + H_2 + O_2 + H (Figures 10 and 11) atmospheres, the last model being our most sophisticated, as it includes thermal and nonthermal collisions as well as interactions with photons and magnetospheric electrons. [b]See Section 2.2 for the description of these scenarios. [c]See Section 1 and CM20 and CM21 for a more thorough description. [d]The upper bound and lower bound correspond to H being produced solely via photodissociation and via photo-impact and electron-impact-induced dissociation, respectively (e.g., Figure 6). [e]When H_2O is the primary source of H, the H corona observed by HST/STIS cannot be reproduced (e.g., Figures 8a–8c and 9). [f]When H_2 is the primary source of H, the H corona observed by HST/STIS can be reproduced (e.g., Figures 8c, 8d, 10a and 10b). Note minor contributions *off the disk* from reflected sunlight (e.g., Figures 8c, 8d, 10a and 10b) and the H produced from H_2O (e.g., Figures 10a and 10b), which is constrained to a peak sublimation flux of $\lesssim10^{12}$ H_2O cm^{-2} s^{-1} and peak number density of $\lesssim10^8$ H_2O cm^{-3}, are included (e.g., Figures 8d and 10b). [g]See corresponding reaction rates in Table B1 in Appendix B.

where ε is the emissivity and, as has been done in the literature at Callisto (Grundy et al., 1999; Moore et al., 1999; Purves & Pilcher, 1980; Sieveka & Johnson, 1982; Spencer, 1987b; Spencer & Maloney, 1984), is assumed to be unity; σ is the Stefan-Boltzmann constant; $A = 0.13$ is the Bond albedo consistent with the literature (Buratti, 1991; Johnson, 1978; Morrison, 1977; Spencer et al., 1989; Squyres, 1980; Squyres & Veverka, 1981); and F is the solar flux at 5.2 AU. Applying Equation 1 at SSL = 0° results in a subsolar temperature of ∼167 K. To resemble the observed temperature maps of Callisto (Hanel et al., 1979; Moore et al., 2004; Spencer, 1987c) reproduced in Figure 1, a minimum temperature of 80 K is enforced at the terminator and the night-side, $T_{\text{night-side}}$ (solid black lines in Figure 1).

2.2.2. Segregated Patches

Assuming the bright ice and dark nonice or ice-poor material is segregated, to generate a temperature distribution for the segregated ice patches, T_{ice} (blue line in Figure 1), according to the disk-averaged ice temperatures derived by Grundy et al. (1999) we assume a constant A and unit emissivity and ignore any longitudinal variations so that the radiative equilibrium equation can be integrated across the day-side hemisphere

$$\int_0^{\pi/2} \left\{ \sigma T_{\text{ice}}^4(\text{SSL}) = (1 - A)F \cos(\text{SSL}) \right\} \sin(\text{SSL}) d\text{SSL} \to \sigma < T_{\text{ice}}^4 >= \frac{1}{2}(1 - A)F \quad (2)$$

where $< >$ represents the hemispheric average. A hemispheric average temperature for the ice can then be calculated as $T_{\text{ice,avg}} = < T_{\text{ice}} >^{1/4} = \left(\frac{(1-A)F}{2\sigma} \right)^{1/4}$. At SSL = 0°, the subsolar (SS) ice temperature, $T_{\text{ice,SS}} = \frac{(1-A)F}{\sigma} = 2^{1/4} T_{\text{ice,avg}}$, and we apply the disk-averaged temperature of ice at Callisto derived by Grundy et al. (1999) for $T_{\text{ice,avg}}$, 115 K, such that $T_{\text{ice,SS}} \sim 137$ K. Note we just use one value for $T_{\text{ice,avg}}$, thereby neglecting the small differences in $T_{\text{ice,avg}}$ (Grundy et al., 1999) calculated between LH and TH and do not consider the lower and upper bounds given by the error bars (±∼20 K). To calculate a day-side surface temperature distribution for the ice patches we use the following equation:

$$T_{\text{ice}}(\text{SSL}) = \left(T_{\text{ice,SS}} - T_{\text{night-side}} \right) (\cos(\text{SSL}))^{1/4} + T_{\text{night-side}} \quad (3)$$

where, like the surface temperature distribution for T_{dark}, $T_{\text{night-side}} = 80$ K is set as a constant at the terminator and the night-side (solid black lines in Figure 1). The surface temperature distribution for the dark nonice or ice-poor patches in this scenario is the same as that calculated above for T_{dark} via Equation 1.

2.3. Sources and Sinks

2.3.1. Sublimation and Thermal Desorption

For the IM scenario, i.e., sublimation from "dirty ice," the spatial distribution of the H_2O sublimation flux corresponding to $T_{\text{dark}}(\text{SSL})$ is reduced by a factor f. Here, f is a fit parameter used to constrain H_2O production and hence its contribution to the observed H corona. In CM21, f was referred to as an "ice concentration," and a value of $f = 10^{-1}$ was used. Since the subsolar temperature applied here, ∼167 K, is roughly 12 K higher than that in CM21, 155 K, we consider a range for $f = 10^{-4} - 10^{-2}$, with the upper bound yielding similar day-side sublimation fluxes and H_2O densities as CM21.

For the SP scenario, when simulating sublimation from segregated ice patches, f represents the surficial coverage of ice, for which we use a conservative estimate from the literature of 10% (Spencer, 1987a). Although the actual size and location of these patches can certainly have an effect on the corresponding sublimation flux and distribution, due to the lack of locally accurate resolution for such parameters, we simply assume a random distribution for the ice throughout the surface where H_2O molecules can sublimate from and return to.

The vapor pressure, P_v, is calculated using the formula from Feistel and Wagner (2007)

$$\ln\left(\frac{P_v(T_0(\text{SSL}))}{P_t} \right) = \frac{3}{2} \ln\left(\frac{T_0(\text{SSL})}{T_t} \right) + \left(1 - \frac{T_t}{T_0(\text{SSL})} \right) \eta\left(\frac{T_0(\text{SSL})}{T_t} \right) \quad (4)$$

where $P_t = 6.1166 \times 10^{-3}$ bar and $T_t = 273$ K are the triple point pressure and temperature for water, respectively; and η is a polynomial relation between the surface temperature, T_0, and T_r. Depending on the sublimation scenario, T_0 can either represent T_{dark}(SSL) (IM) or T_{ice}(SSL) (SP) illustrated in Figure 1 by red and blue lines, respectively. The corresponding sublimation flux, Φ_{subl}, is then calculated via the following equation:

$$\Phi_{\mathrm{subl}} = \frac{P_v}{\sqrt{2\pi k_B T_0 m_{\mathrm{H_2O}}}} f \qquad (5)$$

where k_B is the Boltzmann constant and $m_{\mathrm{H_2O}} = 18.02$ amu is the mass of an H_2O molecule. The sublimation fluxes corresponding to T_{dark}(SSL) (IM) and T_{ice}(SSL) (SP) are illustrated in Figure 2 by solid, dashed, and dash-dotted red lines and a solid blue line, respectively. Note that due to the more gradual decrease in T_{ice} across the day-side hemisphere compared to the relatively sharp drop-off of T_{dark} (Figure 1), Φ_{subl} from the former eventually surpasses that of the latter, regardless of f, near the terminator (SSL $\gtrsim 75°$).

Here, we treat the radiolytic H_2 and O_2 components as described in CM20 and CM21: they are assumed to be in steady-state and desorb from the surface with fluxes relative to the local T_0. The surface fluxes, $\Phi_{\mathrm{desorb},i}$, for these species, i, are calculated as $\Phi_{\mathrm{desorb},i} = \frac{1}{4} n_{0,i} v_i$, where $n_{0,i}$ is a prescribed surface density and $v_i = \sqrt{\frac{8 k_B T_0}{\pi m_i}}$ is the Maxwellian speed for each species. For O_2, consistent with values suggested by Cunningham et al. (2015), we implement $n_{0,O_2} \sim 10^9$ cm^{-3}; and for H_2 we consider a range of values from $n_{0,H_2} \sim (0.4–1) \times 10^8$ cm^{-3}, as discussed further below.

Finally, sublimating H_2O and radiolytically produced H_2 and O_2 molecules are injected into the domain from cells along the surface using a cosine distribution with velocities sampled from a Maxwellian flux distribution according to the local T_0 (e.g., Brinkmann, 1970; Smith et al., 1978). As discussed in CM20 and CM21, we assume the regolith is permeated with returning H_2 and O_2; and in the SP scenario, they thermally desorb from both the ice and nonice or ice-poor patches according to the corresponding local surface temperature, T_{ice} or T_{dark}.

2.3.2. Photochemical and Electron-Impact-Induced Reactions

Interactions with photons and magnetospheric electrons ionize and dissociate H_2O and H_2 producing hot H atoms. Because we are focused on tracking the nascent H as a means to reproduce the observed H corona (Roth et al., 2017a), we do not track the other minor products (e.g., O, OH) nor do we consider photochemical and electron-impact-induced reactions with O_2. We also do not consider ionization of H in the atmosphere as our simulations showed they either return to the surface or they escape the atmosphere much faster than they would be ionized via interactions with photons or magnetospheric electrons.

When an H is created, the excess energy of the reaction is distributed between it and the other products conserving energy and momentum. Since these reactions are rare, the density of H is small compared to that of the other thermal species. Therefore, to improve statistics, each time a reaction occurs that produces H from H_2O or H_2, we create 100 H particles, each with a weight 1/100 that of its parent species, and scatter them in random directions.

Table B1 in Appendix B lists the various reactions, their rates, and the excess energies used in our simulations. To estimate the effect of the magnetospheric electrons, we use the number density, n_e, and temperature, $k_B T_e$, derived from *Voyager* measurements by Neubauer (1998): $n_e = 1.1$ cm^{-3} and $k_B T_e = 100$ eV. We assume they can penetrate the extended region of the atmosphere to get a rough upper limit on their effect. However, the local plasma at Callisto is highly variable (e.g., Galli et al., 2022 and references therein) and both temperature and density are not well constrained. Nevertheless, using, e.g., the range of smaller electron densities from Kivelson et al. (2004) would not affect our principal conclusions.

Ignoring any contribution from ionization plus recombination in the ionosphere, we use the excess energies producing hot H by photon-induced dissociation and ionization from Huebner and Mukherjee (2015). The excess energies resulting in hot H produced by electron impacts are much less certain. If electron energies are low, $\lesssim 16.5$ eV, it is often assumed that they only excite the lowest dissociation state of H_2 and as a result, the energy released is similar to that of the analogous photon-induced dissociation (Reaction 9 in Table B1 in Appendix B); for $k_B T_e \sim 100$ eV, however, the H_2 can be highly excited producing lower energy H fragments (Tseng et al., 2013). Therefore, following Tseng et al. (2013), we use the same excess energy for the electron-impact-induced dissociation as that for the photochemical reaction which produces Lyman-α from H_2 (Reaction 10 in Table B1 in

Appendix B): 0.488 eV. Because there are insufficient data for the other electron-impact-induced reactions, we use, as typically is the case (e.g., Leblanc et al., 2017; Marconi, 2007; Turc et al., 2014), the excess energies from the analogous photochemical processes.

For each particle over every Δt a reaction occurs if a random number between 0 and 1 is less than the total probability of any reaction occurring, $P_{\text{react}} = 1 - \exp\left(-\Sigma_i^N k_{\text{react},i} \Delta t\right)$, where $k_{\text{react},i}$ is the reaction rate of the ith reaction and N is the total number of reactions. The specific reaction is then selected when another random number between 0 and 1 is eventually less than the sequential ratio $P_{\text{react},j} = \Sigma_i^j k_{\text{react},i} / \Sigma_i^N k_{\text{react},i}$, where j represents the first reaction for which the random number is less than $P_{\text{react},j}$. In the cases where we consider electron-impact-induced reactions, since electrons can rapidly move up and down the magnetic field lines continuously flowing past Callisto, we assume for simplicity that electron-impact-induced reactions can occur uniformly throughout Callisto's atmosphere. However, photochemical reactions cannot occur in Callisto's shadow; i.e., when $\cos(\text{SSL}_p) < 0$ and $r_p \sin(\text{SSL}_p) < R_C$. Therefore, because the induced reactions differ spatially, we consider them separately; e.g., after first moving a particle and determining if it collides with others, we sequentially determine if a photochemical reaction occurs and, if not, if an electron-impact-induced reaction occurs.

The cases for which only photochemical production of H occurs are relevant to either effective ionospheric shielding from the electrons (e.g., Strobel et al., 2002) and/or Callisto being well outside of Jupiter's plasma sheet. Note that even if Callisto's ionosphere is present but is predominantly produced by a dense, near-surface O_2 atmosphere (e.g., Kliore et al., 2002), then the corresponding ionopause would also remain close to (i.e., a few tens of kilometers above) the surface so that an extended (e.g., hundreds to thousands of kilometers) H_2 component would not be well shielded from the impinging thermal plasma regardless. Since Callisto's ionosphere has been observed to be transient (Kliore et al., 2002), we also consider interactions with magnetospheric electrons uninhibited by any shielding assuming Callisto is in the center of the plasma sheet as an upper limit for the corresponding contribution to the H corona.

The UV emissions detected by Cunningham et al. (2015) were interpreted as photoelectron excited emissions (i.e., airglow). Liang et al. (2005) also showed photoelectron-induced reactions to be crucial to reproduce the observed electron densities of Kliore et al. (2002) while satisfying the observational constraints of Strobel et al. (2002). When simulating the generation of the H corona from the molecular atmosphere we ignored the photoelectrons, which would a have completely different spatial distribution and a much lower average temperature than the magnetospheric electrons.

2.3.3. Boundary Conditions

All particles that cross Callisto's Hill sphere at r_{max} are assumed to escape from the atmosphere and are removed from the simulation. The surface is assumed to be a source for H_2O, O_2, and H_2 as discussed above, and a sink for these species as well as for H. That is, particles returning to the surface are removed from the simulation as they are assumed to permeate the regolith (e.g., CM20, CM21) and/or react therein. However, we treat the returning H_2O particles slightly differently depending on the assumed surface composition: IM or SP. In the SP scenario, we consider two different boundary conditions as upper and lower limits for the H_2O molecules returning to the surface.

1. "All Return": all particles are removed from the simulation regardless of the material they land on; if they land on an ice patch they are assumed to condense, and if they land on a nonice or ice-poor patch they are assumed to permeate this porous regolith and do not redesorb.
2. "Ice Return": if a random number between 0 and 1 is less than the surficial coverage of ice, 10%, then the particle is assumed to have landed on an ice patch and is removed from the simulation; otherwise it is reemitted at the local $T_{\text{dark}}(\text{SSL})$ after a temperature-dependent residence time, Δt_{res}, as illustrated in Figure C1 in Appendix C.

Since we do not assume that there are any ice patches on which H_2O particles can condense in the IM scenario, but instead that the entire surface is a radiation-altered, porous regolith, as in the "All Return" case in the SP scenario when H_2O particles return to the nonice or ice-poor patches, all returning H_2O particles are assumed to permeate this material and do not redesorb.

2.4. Treatment of Hubble Data and Forward Model

To analyze the likelihood of the scenarios considered, we compare the simulation results with the HST/STIS observation at Lyman-α at eastern elongation reported by Roth et al. (2017a). To do so, we generate a slightly modified version of the forward model used in Roth et al. (2017a) and Alday et al. (2017) to recreate the brightness at Lyman-α observed by HST/STIS. Here, we provide a summary of the main characteristics of the forward model, but a more thorough description can be found in those references.

The H number density from the DSMC simulation for each scenario is integrated along the LOS in the 2D grid illustrated in Figure A2 in Appendix A. The resultant H LOS column density, N_H, is then converted into a coronal brightness using $I_H = 10^{-6} \cdot N_H \cdot g$, where 10^{-6} is a scaling factor for the unit conversion to Rayleigh and g is the photon scattering coefficient (or g-factor), which allows for the calculation of the resonant scattering of solar photons by H atoms (Chamberlain & Hunten, 1987). Here, we set $g = 1.24 \times 10^{-4}$ s^{-1}, the value calculated by Roth et al. (2017a) at eastern elongation using the line center solar irradiance for the day of the HST/STIS observation. The simulated H coronal brightness is then combined with sunlight reflected off Callisto's surface, the brightness of the interplanetary medium, as well as the airglow of the Earth's geocorona, with the latter two derived from the HST/STIS data (Roth et al., 2017a). Thus, we considered all possible backgrounds for the comparison to the HST observation and present only reasonable assumption and fits.

In addition, we consider the absorption of Lyman-α photons by the H_2O atmospheric component, which can be nonnegligible for scenarios with high water vapor abundances (Roth et al., 2017b). The combination of these parameters allows us to generate a 2D Lyman-α brightness image that is finally convolved with the instrument point spread function (Krist et al., 2011) to take into account the instrumental effects (Alday et al., 2017; Roth et al., 2014).

To compare the forward model with the observed HST/STIS image, we average the simulated and observed 2D images using radial bins to generate 1D profiles of Lyman-α brightness as a function of radial distance from Callisto's center. Radial averaging implies that the number of averaged pixels within each bin increases with distance from the center. As a result, the bin at the center has the least number of averaged pixels, leading to a large statistical uncertainty (i.e., large error bar) of the HST/STIS profile in this region. Therefore, we set the radius of the bin at the center to $0.15R_C$ to improve the statistics, while every radial bin thereafter has a radius of $0.1R_C$.

Finally, while the H contribution to the forward model is directly fed from the simulations, the surface albedo at Lyman-α, which is required to model the contribution from the reflected sunlight off Callisto's surface, is not known. To estimate it, equivalent to the approach used by Roth et al. (2017a), we use a Levenberg-Marquardt algorithm to minimize the difference between the simulated and measured intensities and fit the surface albedo. However, because the atmospheric signals overlap with surface reflections on the disk, the region off the disk (just above the limb) contains the most reliable data points for constraining the contributions to the H corona. That means the off-disk signal, and in particular the signal at all points more than 3 pixels ($\sim$200 km) away from the limb, is not affected by any uncertainties in modeling the reflectance signal.

3. Results

We simulate Callisto's atmosphere in 2D using the DSMC method (Bird, 1994) to examine the roles of sublimated H_2O and radiolytically produced H_2 as sources of the H corona observed by HST/STIS at eastern elongation (Roth et al., 2017a) by modeling the nascent H produced by their interactions with photons and magnetospheric electrons. Our goal is to place constraints on the surface source rates and resultant densities for H_2O and H_2. A summary of the components of and the corresponding assumptions implemented in the simulated atmospheres presented below can be found in Table 1. Physical parameters of Callisto used in various calculations below are listed in Table D1 in Appendix D.

3.1. H From H_2O

For an icy surface whose composition is an IM, sublimation of H_2O is determined by an assumed water ice concentration, which we represent with a sublimation reduction factor, f, and the local surface temperature, T_{dark}. Consistent with similar simulations in CM21, by applying the results in Figure 2 the corresponding H_2O
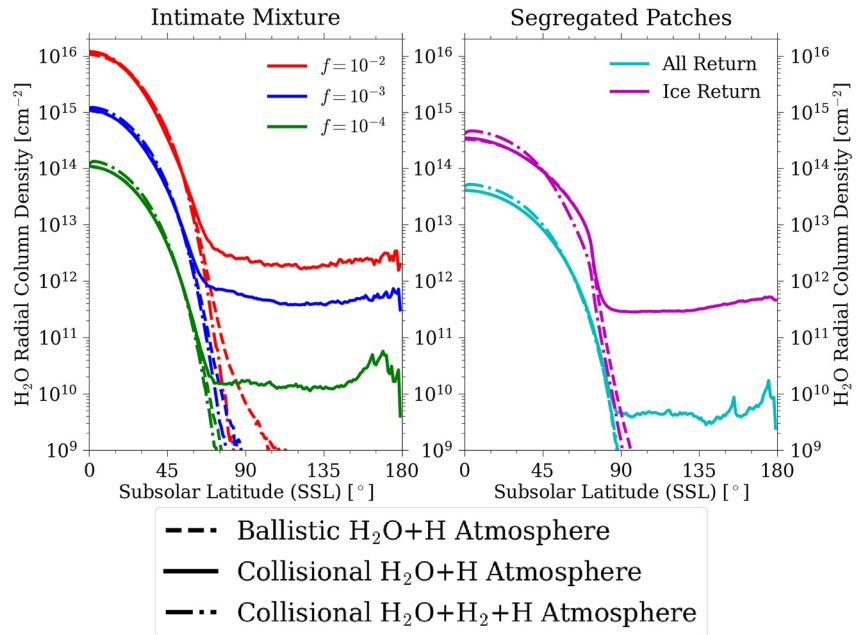
Figure 3. H_2O radial column densities generated in the intimate mixture and segregated patches simulations. f is the sublimation reduction factor implemented in the former (Section 2.3.1), which varies from 10^{-2} (red lines) to 10^{-3} (blue lines) to 10^{-4} (green lines), and "All Return" (cyan lines) and "Ice Return" (magenta lines) represent the boundary conditions enforced in the latter (Section 2.3.3). Solid and dashed lines represent simulations where $H_2O + H$ collisions were considered and neglected in an $H_2O + H$ atmosphere, respectively, and dash-dotted lines represent atmospheres where collisions with H_2 assuming $n_{0,H_2} \sim 10^8 \, cm^{-3}$ were also considered.

atmosphere is most dense near the subsolar point, and drops off several orders of magnitude as one approaches the terminator (Figure 3). For an icy surface with SP where sublimation of H_2O solely occurs from relatively cold ice patches covering only 10% of the surface at the local ice temperature, T_{ice}, by applying the result in Figure 2 the distributions are similar to those in the IM model, but the peak densities near the subsolar point can be much less, albeit if H_2O molecules are able to redesorb back into the atmosphere, the density can be enhanced roughly an order of magnitude due to the diminished loss rate to the surface (cyan versus magenta lines in Figure 3). Since the local temperature in the IM model is determined by the dark material and, as a result, is much warmer than the bright ice patches (e.g., Figure 1: at SSL = 0°, T_{dark} is ~30 K warmer than T_{ice}) it is not surprising that it can exhibit orders of magnitude larger densities depending on the ice concentration. In addition, implementing a temperature-dependent residence time, Δt_{res}, effectively halts the H_2O migration for SP beyond SSL $\gtrsim 75°$, where Δt_{res} is on the order of Callisto's orbital period, $t_{orb} \sim 1.44 \times 10^6$ s (Figure C1 in Appendix C). That is, there is no further migration beyond this region for returning particles, and as a result, there is a sharp drop-off in density thereafter.

In a single-species H_2O atmosphere for either sublimation scenario, consistent with CM21, including or neglecting $H_2 + H_2O$ collisions, has a negligible effect on the density distribution. In an $H_2O + H$ atmosphere, however, $H_2O + H$ collisions can transfer enough energy to the H_2O molecules to reach the night-side, thereby populating a night-side H_2O atmosphere (Figure 3), and the loss of H_2O slightly increases due to nonthermal escape. However, when a thermal H_2 component with $n_{0,H_2} \sim 10^8 \, cm^{-3}$ is included, $H_2O + H_2$ collisions quench the nonthermal H_2O produced by collisions with the hot H, diminishing any night-side H_2O component and inhibiting any escape. These features can be seen when comparing the solid, dashed, and dashed-dotted lines in Figure 3 as follows. The lines representing ballistic $H_2O + H$ atmospheres (dashed lines), collisional $H_2O + H$ atmospheres (solid line), and collisional $H_2O + H_2 + H$ (dashed-dotted lines) effectively coincide until close to the terminator. Beyond the terminator the solid lines remain relatively flat as a result of H_2O molecules migrating to the night-side and/or escaping after colliding with hot H atoms. Conversely, the dashed and dashed-dotted lines sharply drop-off prior to the terminator, the former is because H_2O molecules simply follow ballistic trajectories and do not interact with the hot H atoms and the latter is because the H_2 component fully quenches the nonthermal energy from the H_2O molecules via collisions. When n_{0,H_2} is reduced to $\sim 4 \times 10^7 \, cm^{-3}$, the influence of H_2 is reduced; e.g., the
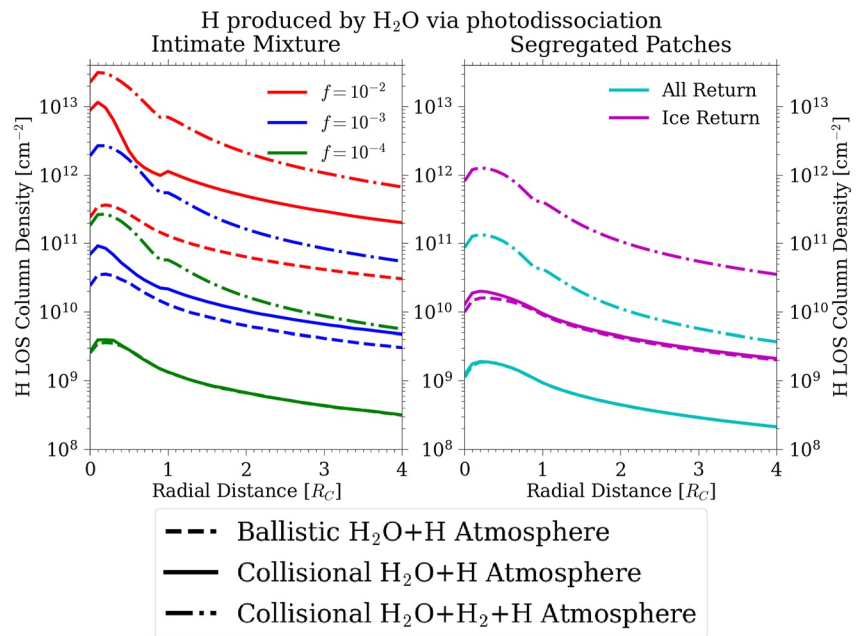
Figure 4. H line-of-sight (LOS) column densities generated in the intimate mixture and segregated patches simulations. f is the sublimation reduction factor implemented in the former (Section 2.3.1), which varies from 10^{-2} (red lines) to 10^{-3} (blue lines) to 10^{-4} (green lines), and "All Return" (cyan lines) and "Ice Return" (magenta lines) represent the boundary conditions enforced in the latter (Section 2.3.3). Solid and dashed lines represent simulations where $H_2O + H$ collisions were considered and neglected in an $H_2O + H$ atmosphere, respectively, and dash-dotted lines represent atmospheres where collisions with H_2 assuming $n_{0,H_2} \sim 10^8$ cm^{-3} were also considered. As can be seen, with increasing f (and hence H_2O density), the H density increases as it diffuses through this collisional component, and the H density increases even more when the collisional H_2 component is included. Note the scale for the LOS column densities are the same as in Figure 6 for comparison. The dip in LOS column density at the center of the disk is an artifact of using radial bins for the density simulations and azimuthal bins for the LOS estimate.

nonthermal energy transferred via $H_2O + H$ collisions is not fully quenched by $H_2O + H_2$ collisions, and as a result, H_2O is able to migrate to the night-side as well as escape. Similarly, the nonthermal energy transferred via $O_2 + H$ collisions induces O_2 escape.

Using the parameters in Table B1 in Appendix B, magnetospheric electron-impact dissociation of H_2O, producing either one or two H, has a much smaller influence on the net production of H relative to photochemical production. The spatial morphology of H from H_2O, regardless of the sublimation scenario, has a similar spatial distribution as its parent: its density peaks near the subsolar point. Therefore, the LOS column density of H also peaks on the disk ($<1R_C$) and drops off rapidly with increasing distance from the disk (Figure 4). Collisions with the H_2O serve to slow the H down, thereby reducing its average "temperature" (i.e., a measure of the particles' kinetic energy) and enhancing the H density over the disk. Thus, as can be seen in Figure 4, with increasing f (and hence peak H_2O density; e.g., Figure 3), the difference between H LOS column densities in collisional (solid lines) and ballistic (dashed lines) $H_2O + H$ atmospheres increases, especially when a collisional H_2 component is also present (dashed-dotted lines). In a relatively thin H_2O atmosphere, however, such as that produced assuming IM with $f = 10^{-4}$ or SP, the influence of the $H_2O + H$ collisions has a negligible effect on the H component, hence the coinciding solid and dashed green, cyan, and magenta lines in Figure 4. Also, when collisions with thermal molecules in the atmosphere are neglected, the temperature of the H remains roughly isothermal, and is thus determined by the excess energies of the reactions producing it, resulting in temperatures as high as $\sim 10^4$ K. However, when collisions with the thermal molecules are taken into account, these temperatures are cooled significantly in the collisional regime of the atmosphere, becoming comparable to those of the thermal molecules; e.g., as low as $\sim 10^2$ K near the surface.

When H_2 and O_2 are included, the distribution of H from H_2O is significantly affected. With only O_2 also present (e.g., CM21) with $n_{0,O_2} \sim 10^9$ cm^{-3}, it can scatter H atoms that would have otherwise rapidly returned to the surface. Such scattering can redirect H atoms migrating to and descending into the night-side atmosphere upward,
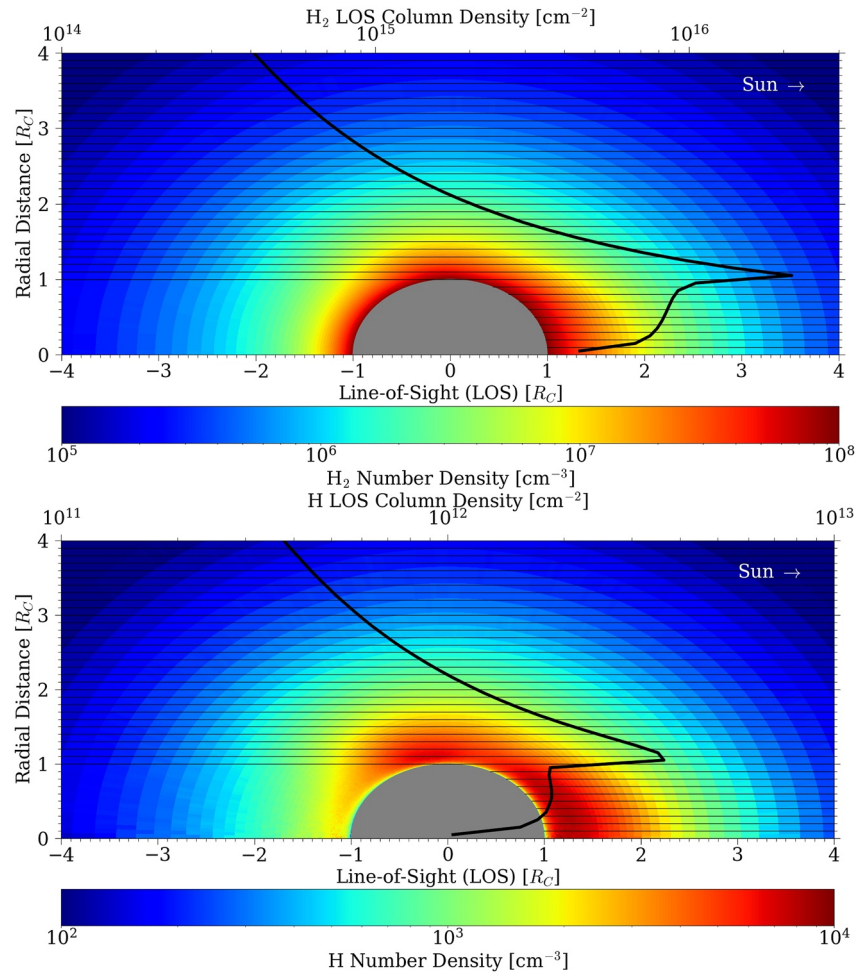
Figure 5. Number densities (color spectrum) and line-of-sight (LOS) column densities (black line; x-axis, *top*) for (a) radiolytically produced H_2 with a surface density of $n_{0,H_2} \sim 10^8$ cm^{-3} and (b) the H it produces via photochemical reactions in an H_2 + H atmosphere. The thin black horizontal lines represent the integration bins in which the LOS column densities are calculated with the Sun located to the right of the plot (positive x-direction). The dip in the LOS column densities at the center of the disk is a numerical artifact (see caption of Figure 4).

producing a secondary peak away from the subsolar point, albeit it is much smaller than the primary peak in the subsolar region where the H is primarily produced. When an H_2 component with $n_{0,H_2} \sim 10^8$ cm^{-3} is also included, not only is the nonthermal energy of the H_2O quenched via $H_2O + H_2$ collisions, which diminishes its night-side density and inhibits its escape (dash-dotted lines in Figure 3), but the density of the H produced from H_2O can be further enhanced relative to when only H_2O is present by more than an order of magnitude (solid versus dash-dotted lines in Figure 4). This is due to H_2 becoming the dominant collision partner relatively close to the surface, $\lesssim 100$ km (e.g., CM21), so that any H produced from H_2O has to diffuse through this collisional component en route to returning to the surface or escaping.

3.2. H From H_2

A range of steady-state simulations were carried out that only include H_2 and H produced by photodissociation and then by photo-impact and electron-impact-induced dissociation. Results are discussed for $n_{0,H_2} \sim 10^8$ cm^{-3}, where only interactions with photons are considered, and for $n_{0,H_2} \sim 4 \times 10^7$ cm^{-3}, the "intermediate" case from CM21, where interactions with both photons and magnetospheric electrons are considered. The results from the former are illustrated in Figure 5 with an IM surface, which is very similar to that with an SP surface.
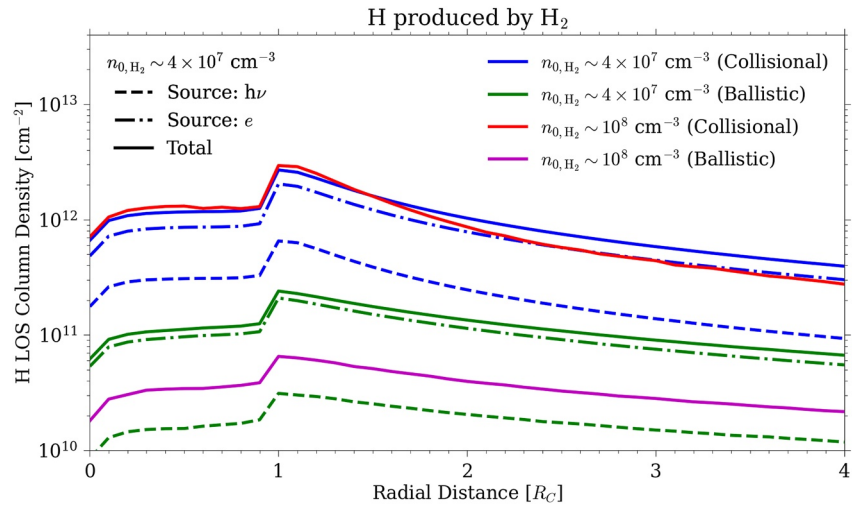
Figure 6. H line-of-sight (LOS) column densities generated in $H_2 + H$ atmospheres, where H is produced via interactions with photons ($h\nu$) only with $n_{0,H_2} \sim 10^8$ cm^{-3} (red and magenta lines) and via interactions with $h\nu$ and magnetospheric electrons (e) with $n_{0,H_2} \sim 4 \times 10^7$ cm^{-3} (blue and green lines). For the latter, the dashed and dash-dotted lines represent H produced via interactions with $h\nu$ and e, respectively, and the solid lines represent the sum total of H. The red solid line and blue lines represent simulations where $H_2 + H$ collisions were considered and the magenta solid line and green lines represent simulations where they were neglected. Note the scale for the LOS column densities are the same as in Figure 4 for comparison. The dip in the LOS column densities at the center of the disk is a numerical artifact (see caption of Figure 4).

As can be seen in Figure 5, although the distributions of H_2 (top panel) and H (bottom panel) are global, both species exhibit density peaks on the day-side. Whereas the relatively small day/night asymmetry for H_2 is a result of the diurnal surface temperature gradient, when H is produced only by photodissociation the asymmetry is due to the lack of production in Callisto's shadow. For both H_2 and H, the sharp peak in the LOS distribution occurs just off Callisto's limb (1–$1.1 R_C$) as expected for a species with a global distribution (e.g., Roth et al., 2017a). As a result, these simulated LOS profiles are similar to that estimated by Roth et al. (2017a) with a slope proportional to the inverse of the radial distance from Callisto squared.

As shown in Figure 6, with the electron-impact-induced reaction rates in Table B1 in Appendix B, the amount of H_2 required to produce the same amount of H is reduced by about 2.5, from $n_{0,H_2} \sim 10^8$ cm^{-3} (solid red line) to $\sim 0.4 \times 10^8$ cm^{-3} (solid blue line). Better constraints on the influence of magnetospheric electrons at Callisto's orbit are, of course, needed. Finally, LOS profiles of H were calculated ignoring hot H collisions with H_2, as in ballistic calculations of a corona, or including them, as in molecular kinetic models. Although the shape of all of the H LOS column density profiles in Figure 6 is very similar, it is seen that such collisions can enhance the H component as described in Section 3.1 by more than an order of magnitude (red versus magenta line, blue versus green lines).

Photoabsorption in an H_2 component with a surface density of $n_{0,H_2} \sim 10^8$ cm^{-3} can diminish photodissociation (and hence H production) rates with increasing depth into the atmosphere. We estimated this effect as follows. The H production rate is obtained by first integrating the H_2 density along the LOS (x-axis in Figure A2 in Appendix A) obtaining the local LOS column density penetrated as a function of depth, which also varies with radial distance from the LOS (y-axis in Figure A2 in Appendix A), $N(x, y)$. The dissociation rate for each reaction, i, becomes $\nu_i \exp(-N(x, y)\sigma_{abs,i})$, where $\sigma_{abs,i}$ is the relevant photoabsorption cross-section for the processes, ν_i, in Table B1 in Appendix B; ν_i and $\sigma_{abs,i}$ are illustrated as a function of the wavelength in Figure E1 in Appendix E. Figure 7 shows that at most $\sim 13\%$ of the incoming photon flux is absorbed near the terminator. However, the opacity in this relatively dense H_2 atmosphere is even less of an issue when magnetospheric electrons are considered since the H_2 density required to reproduce the H corona is reduced (Figure 6).

When collisional H_2O and/or O_2 components are included they affect the spatial distribution of H_2, which in turn affects the spatial distribution of the H produced. Based on our constraints discussed below, H_2O only affects H_2 in the subsolar region, whereas its interactions with a more dense O_2 component dominates globally, albeit the average density of O_2 is not well constrained. As both species affect the H_2 in the subsolar region, the LOS
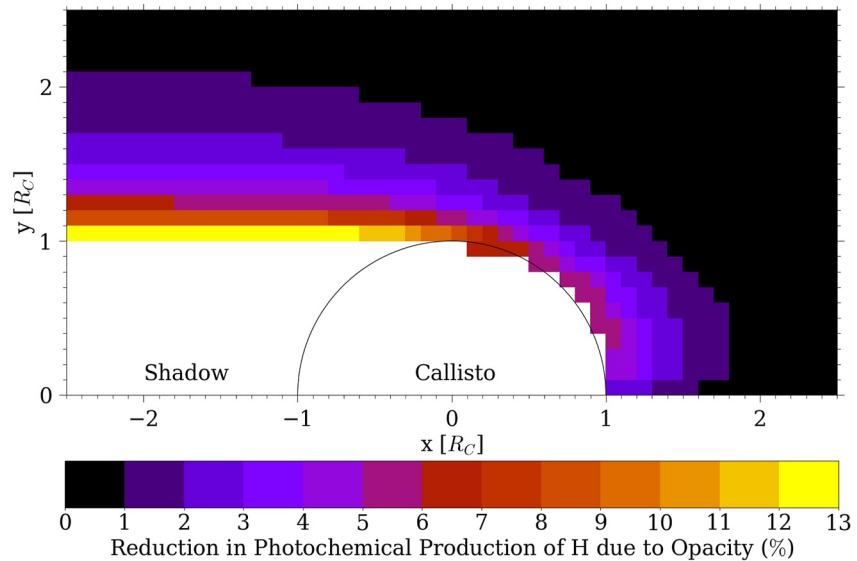
Figure 7. Percent reduction in the photochemical production of H from H_2 with a surface density of $n_{0,H_2} \sim 10^8$ cm^{-3} due to opacity using the wavelength-dependent absorption cross-sections and reaction rates illustrated in Figure E1 in Appendix E.

column densities of the H_2 and the H it produces beyond the terminators are only slightly affected. That is, collisions with the heavier thermal species can limit the outflow and migration of H_2 on the day-side, which inhibits its migration to and heating and inflation of the night-side atmosphere (e.g., CM21). Since the H distribution primarily follows that of its parent species it is similarly affected.

3.3. H Corona: Comparison to Hubble Observation

For an H_2O + H atmosphere using the IM scenario assuming $f = 10^{-2}$, the total modeled corona brightness is seen in Figure 8a to exceed the total observed brightness near the subsolar point, where the production of H atoms from H_2O peaks. This is the case even when considering the depletion of Lyman-α flux via absorption by the H_2O molecules, as indicated by the dip in reflected sunlight in the center of the disk (Figure 8a). On the other hand, due to the rapid decrease in sublimation away from the subsolar point, the production of H is too small to replicate the observed brightness beyond the terminator ($>1R_C$; dark blue line in Figure 8d), which is also true for the SP models, where there is no depletion of Lyman-α on the disk (Figure 8b) and the production of H is even smaller (light blue line in Figure 8d). On the other hand, the distribution of H produced from H_2 assuming $n_{0,H_2} \sim 10^8$ cm^{-3} over the disk, although relatively small relative to the reflected sunlight, is more uniform, increasing from the center of the disk to the terminator until reaching a maximum just off the disk (Figure 8c) as in the LOS column density distributions of H_2 and H (Figures 5 and 6). The combination of the reflected sunlight and the brightness of the H corona produced from H_2 provide a good fit to the HST/STIS measurement (red line in Figure 8d).

In addition to scenarios in which H is solely produced from one of the parent species, we also simulated cases including both H_2O and H_2 as sources of H via interactions with photons and magnetospheric electrons as well as collisions with an O_2 component with $n_{0,O_2} \sim 10^9$ cm^{-3}. For the IM case a good fit to the data requires $f \lesssim 10^{-3}$ because with a larger f the modeled brightness over the disk becomes even more problematic when collisions with other components are considered (e.g., Figure 9), which can create an even larger brightness peak than that in Figure 8a and is thus inconsistent with the relatively flat disk profile in the HST/STIS data. However, if f is reduced to improve the agreement over the disk (Figure 10a), then the H produced from H_2O off the disk is $\sim 5\times$ less than that observed (Figure 10b). Therefore, the inconsistencies of H_2O producing too much H near the subsolar point and too few H away from Callisto's disk relative to the observed H morphology affirm that the H_2 component with an average surface density of $n_{0,H_2} \sim 4 \times 10^7$ cm^{-3} is the primary producer of the morphology of the observed H, with minor contributions off the disk from the reflected sunlight and H from H_2O (Figure 10b). For the SP cases, the contribution to the brightness by H produced from H_2O is even smaller off the disk (e.g.,
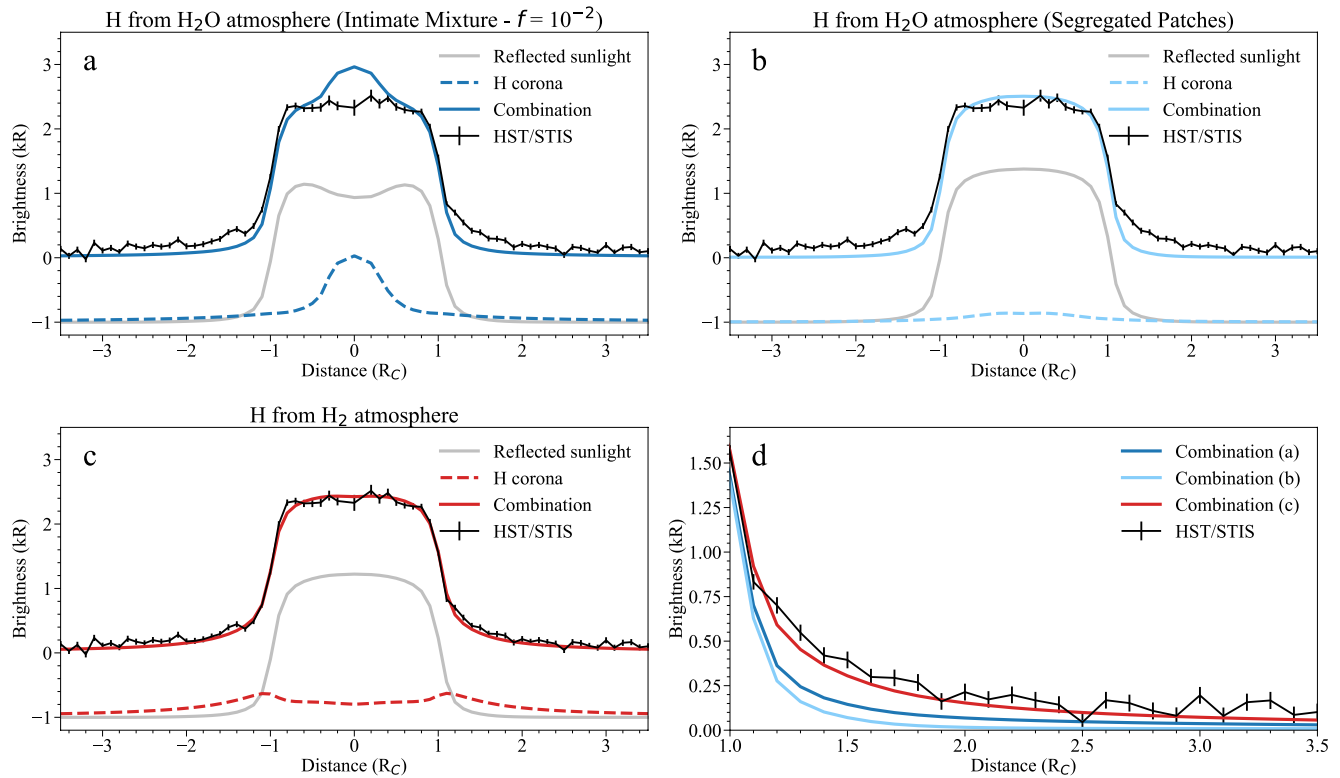
Figure 8. Comparison of the HST/STIS observation with the simulation results for the cases of an H corona produced via photodissociation from H_2O in the (a) intimate mixture with $f = 10^{-2}$ and (b) segregated patches, Ice Return sublimation scenarios, as well as (c) via photodissociation from radiolytically produced H_2 with $n_{0,H_2} \sim 10^8$ cm^{-3}. The coronal brightness in (a), (b), and (c) are represented by dark blue, light blue, and red dashed lines, respectively; the black line represents the measured HST/STIS Lyman-α profile with black vertical segments for error bars of the measurement; the gray line represents the contribution from reflected sunlight; and the forward model results are represented by solid lines of the same color of the coronal brightness. The reflected sunlight in (a) and (b) also includes the absorption at Lyman-α by H_2O molecules, hence the dip in at the center of the disk in (a). The reflected sunlight and coronal emissions in (a)–(c) are offset by -1 kR to improve the visibility of the figure. Panel d shows a closer look at the forward model results for all cases near the terminator, where the sensitivity of the HST/STIS observation to the H corona is highest. Whereas the axisymmetric simulation results are the same on either side of Callisto's disk, the HST/STIS data presented in (d) are the average of the values from $-1 \rightarrow -3.5R_C$ and $1 \rightarrow 3.5R_C$.

Figure 8d), so the observed data are also predominantly due to surface reflection on the disk and H produced from H_2 off the disk. For either case, SP or IM with $f \lesssim 10^{-3}$, although the brightness off the disk is dominated by the H produced from H_2, the contributions on the disk are obscured by Lyman-α reflection. That is, any reduction in coronal brightness over the disk does not significantly affect the comparison to the observation, whereas off the disk the comparison is crucial (see Section 2.4).

As described in Section 2.4, we assumed the g-factor calculated by Roth et al. (2017a) when converting the simulated H abundances to the brightness of the scattered sunlight. We estimate an uncertainty of up to 30%, factoring in, e.g., the variability of the solar intensity and simplifications about the resonant scattering properties (neglecting all optical thickness effects). Comparing the g-factor from Roth et al. (2017a) to the scaled Lyman-alpha g-factors from Killen et al. (2009), the latter are about 25% lower (when scaled with distance from the Sun and daily solar flux) confirming our estimated uncertainty. This $\leq$30% uncertainty translates linearly to the derived abundances everywhere and therefore does not affect our conclusions on the roles of H_2O and H_2 for producing the observed corona profiles on and off the disk. Although it does affect the derived absolute abundances, the 30% range is small compared to the uncertainties introduced from the plasma conditions (see Section 2.3.2) as well as other effects, such as those discussed later in Section 4.2.

As originally suggested in Roth et al. (2017a), a fit to the HST/STIS observation can be generated by a scenario with a nearly uniformly distributed source of H, as is the case in our simulations with H_2. Therefore, we considered other possible sources for the observed H. Using the plasma parameters from Vorburger et al. (2019) (see Tables D3 and D4 in Appendix D), proton charge-exchange with all atmospheric species considered in the models
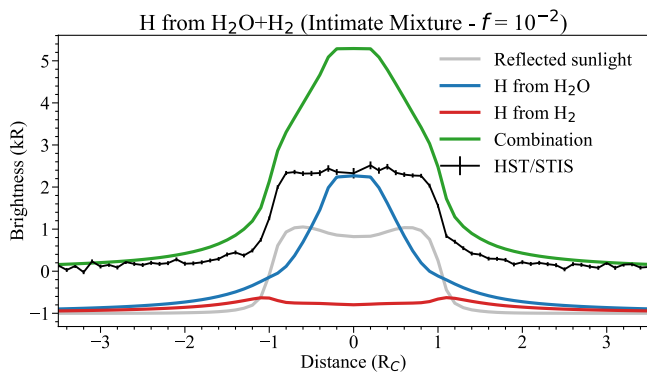
Figure 9. Comparison of the HST/STIS observation with the simulation results for the case of an H corona produced via photodissociation of H_2O (dark blue line) and H_2 (red line) in an $H_2O + H_2 + H$ atmosphere assuming the intimate mixture sublimation scenario with $f = 10^{-2}$ and $n_{0,H_2} \sim 10^8$ cm^{-3}. The black line represents the measured HST/STIS Lyman-α profile with black vertical segments for error bars of the measurement; the gray line represents the contribution from reflected sunlight including the absorption at Lyman-α by H_2O molecules, hence the dip at the center of the disk; and the green line represents results from the forward model. The reflected sunlight and coronal emissions are offset by -1 kR to improve the visibility of the figure.

as well as with the observed CO_2 and O components produces a negligible source rate of H. In addition, Vorburger et al. (2015) assumed H was produced via sputtering from hydrated nonice surface materials; however, the peak number densities they obtained were $\sim 10^0$ cm^{-3} (Figure 3 therein). Thus, there is no sufficient *direct* surface source of H that would reproduce the observation.

In Figures 10 and 11, we present results from our most sophisticated model of Callisto's atmosphere composed of H_2O, H_2, O_2, and H subject to interactions with photons and magnetospheric electrons in which the H_2 component with an average surface density of $n_{0,H_2} \sim 4 \times 10^7$ cm^{-3} is the primary producer of the morphology of the observed H, the H_2O component assuming an IM surface with $f \lesssim 10^{-3}$ is only a minor producer, and the spatial distributions of the atmospheric components are affected by thermal and nonthermal collisions. Our simulation results are dependent on the input parameters we implement, such as the assumed dissociative reaction rates which produce H. However, for the reasons described above, our principal conclusions that H_2 is the primary source of Callisto's H corona and that H_2O cannot be the primary source are not affected by varying such parameters.

4. Discussion and Constraints

Here, we discuss the implications of our results and the rough constraints on sublimation of H_2O and the amount of H_2 produced primarily from radiolysis.

4.1. Sublimated H_2O

When the ice on Callisto's surface is intimately mixed with the dark nonice or ice-poor material and H_2O is assumed to desorb from Callisto's warm, day-side surface at a relatively small fraction of the ice sublimation rate ($f = 10^{-2}$), more than enough H is produced to account for the HST/STIS observation of an H corona at Callisto. However, the spatial distribution of H is not consistent with the observation. That is, the LOS column density of the simulated H peaks near the subsolar point, which is inconsistent with what is seen on the disk by HST/STIS (e.g., Figures 8a and 9), and too few H is produced off the disk (e.g., Figure 8d). Moreover, relatively dense and collisional H_2O and H_2 components *cannot both be present* in Callisto's atmosphere, since as seen in Figure 9 redistribution of the H produced from H_2O via $H_2 + H$ collisions enhances this already large discrepancy. If f is reduced to improve the agreement over the disk, the discrepancy between the H produced from H_2O and what is observed off the disk becomes even worse (Figure 10b). Conversely, increasing f to improve the agreement off the disk results in a discrepancy between the H produced from H_2O and what is observed over the disk (e.g., Figures 8a and 9). This implies that a global source of H is needed so that such a sharp drop-off in local H production and the corresponding density off the disk does not occur, and the emissions on the disk are dominated by sunlight reflected from the surface rather than those from local atmospheric sources. Since, as described above, radiolytically produced H_2 is distributed globally at Callisto, we propose H_2 is this global source of H. Based on the observation over the disk the H_2O peak density must be $\lesssim 10^8$ cm^{-3} requiring that $f \lesssim 10^{-3}$ (e.g., Figure 10). When the ice on Callisto's surface is assumed to be segregated into patches of bright ice and dark nonice or ice-poor material and H_2O is assumed to primarily sublimate from the former at the local ice temperature, the spatial distribution is similar to that for the IM scenario, but the amount of H produced is insufficient to explain the observation (e.g., Figure 8d), even when the H abundance increases via collisions with other species. Therefore, H_2O is not the primary source of the H corona.

The constraint on the peak number density, $\lesssim 10^8$ H_2O cm^{-3}, corresponds to a peak sublimation flux of $\lesssim 10^{12}$ H_2O cm^{-2} s^{-1} (Figure 2) and a peak radial column density of $\lesssim 10^{15}$ H_2O cm^{-2} (Figure 3). These constraints are significantly less than those implemented in the literature: applying a uniform surface temperature of 150 K, Liang et al. (2005) derived a maximum number density of $\sim 2 \times 10^9$ H_2O cm^{-3} (Figure 2 therein); applying a single day-side surface temperature profile with a $T_{max} = 165$ K and a range of ice coverage of $\sim 60\%$–73%, Vorburger et al. (2015) derived a maximum number density of $\sim 4 \times 10^{10}$ H_2O cm^{-3} (Figure 1 therein); applying a maximum
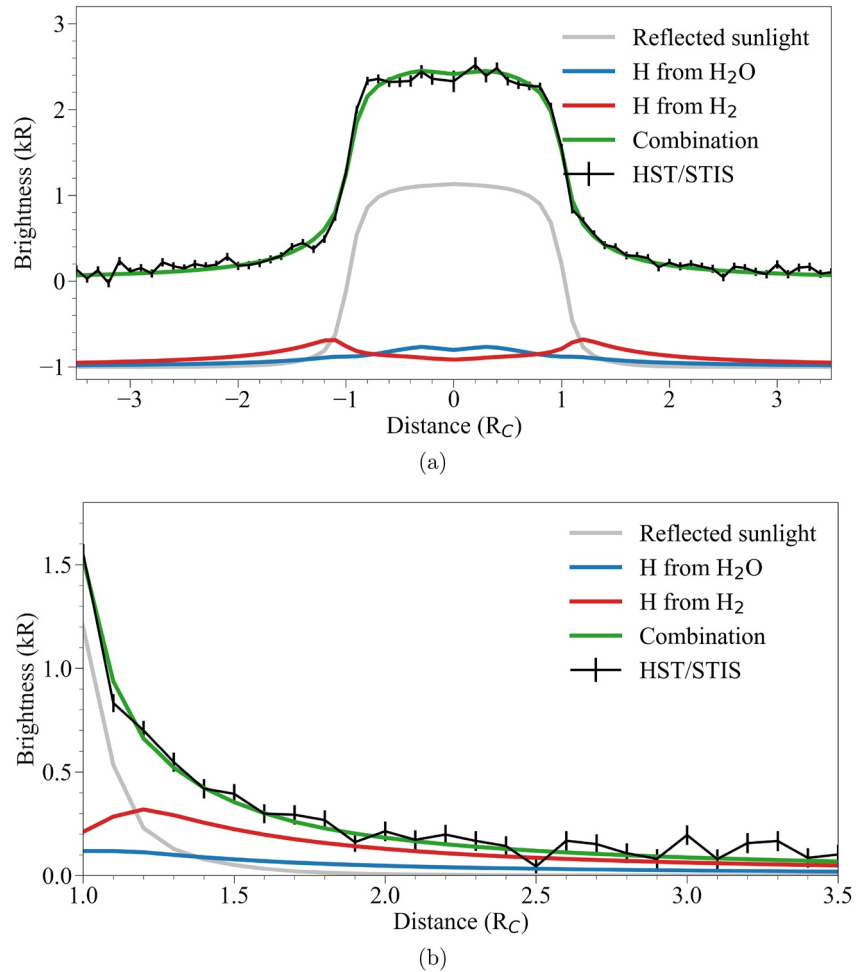
Figure 10. (a) Comparison of the HST/STIS observation with the simulation results from our most sophisticated model of Callisto's atmosphere: an $H_2O + O_2 + H_2 + H$ atmosphere subject to interactions with photons and magnetospheric electrons assuming an intimate mixture (IM) surface, a sublimation reduction factor of $f = 10^{-3}$, and O_2 and H_2 surface densities, n_0, of $\sim10^9$ and $\sim4 \times 10^7$ cm^{-3}, respectively. The H produced from sublimated H_2O and radiolytically produced H_2 are represented by dark blue and red lines, respectively; the black line represents the measured HST/STIS Lyman-α profile with black vertical segments for error bars of the measurement; the gray line represents the contribution from reflected sunlight including the absorption at Lyman-α by H_2O molecules; and the green line represents results from the forward model. The reflected sunlight and coronal emissions are offset by -1 kR to improve the visibility of the figure. (b) A closer look at the results from (a) near the terminator, where the sensitivity of the HST/STIS observation to the H corona is highest. Whereas the axisymmetric simulation results are the same on either side of Callisto's disk, the HST/STIS data presented in (b) are the average of the values from $-1 \rightarrow -3.5R_C$ and $1 \rightarrow 3.5R_C$.

temperature of 155 K, Hartkorn et al. (2017) derived a maximum column density of $\sim3 \times 10^{16}$ H_2O cm^{-2} (Figure 7 therein); and using the temperature distribution from Hartkorn et al. (2017) and $f = 10^{-1}$, CM21 derived a maximum sublimation flux of $\sim10^{13}$ H_2O cm^{-2} s^{-1} (Figure 1 therein), number density of $\sim10^9$ H_2O cm^{-3} (Figure E2 therein), and column density of $\sim8 \times 10^{15}$ H_2O cm^{-2} (also Figure E2 therein). Despite the relatively low fluxes at Callisto considered here, sublimation still produces several orders of magnitude more H_2O than would sputtering of its surface, even when assuming the full magnetospheric particle flux reaches the surface (e.g., Vorburger et al., 2019).

The most recent modeling efforts for Europa suggest sublimation fluxes of $\sim10^{11}$ H_2O cm^{-2} s^{-1} (Plainaki et al., 2018 and references therein), whereas a large range of fluxes have been suggested for Ganymede's "dirty ice" (e.g., Leblanc et al., 2017). While Leblanc et al. (2017) suggested that sublimation from dirty ice could be lower than the lowest bound presented here ($\sim10^8$ H_2O cm^{-2} s^{-1}, Figure 2 therein), they also consider rates even higher than the upper bound considered here ($>10^{15}$ H_2O cm^{-2} s^{-1}, also Figure 2 therein), which yields a column
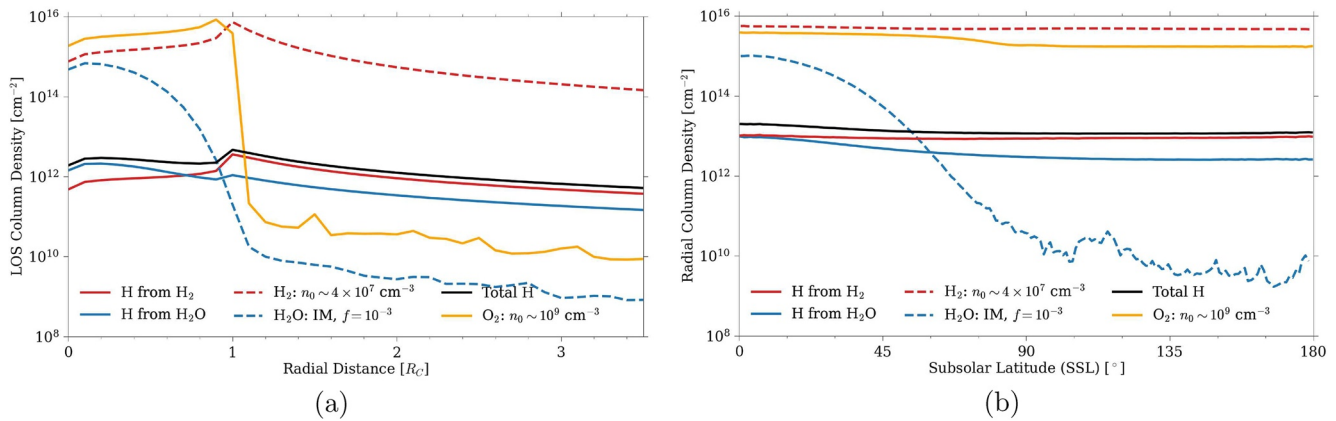
Figure 11. Results from our most sophisticated model of Callisto's atmosphere: an $H_2O + O_2 + H_2 + H$ atmosphere subject to interactions with photons and magnetospheric electrons assuming an intimate mixture (IM) surface, a sublimation reduction factor of $f = 10^{-3}$, and O_2 and H_2 surface densities, n_0, of $\sim 10^9$ and $\sim 4 \times 10^7$ cm^{-3}, respectively. Radial and line-of-sight (LOS) column density profiles are presented in (a) and (b), respectively, with results for H_2O and H_2 presented in dashed dark blue and red lines, respectively, the H they produce in the same colors in solid lines, the total H produced in solid black, and O_2 in orange. From SSL = 0–180°, the average Knudsen number at the surface $Kn_{0,avg} = \frac{\Sigma_i Kn_{0,i} n_{0,i}}{\Sigma_i n_{0,i}} \sim 0.02 - 0.05$, where i represents the species, and $Kn = \ell/H$ is a dimensionless number used to determine the rarefaction of the atmosphere, with ℓ and H the local mean free path and scale height, respectively. With this reduced n_{0,H_2} the nonthermal energy transferred via $H_2O + H$ collisions is not fully quenched by $H_2O + H_2$ collisions so that H_2O molecules are able to migrate to the night-side (a) and escape, resulting in the thin extended component beyond Callisto's disk shown in (b). Similarly, the nonthermal energy transferred via $O_2 + H$ collisions induces O_2 escape resulting in the thin extended component shown in (b). The dip in the LOS column densities at the center of the disk is a numerical artifact (see caption of Figure 4).

density similar to the largest estimate suggested here, $\sim (3–8) \times 10^{15}$ H$_2$O cm^{-2}. Marconi ([2007](#)) estimated an H$_2$O sublimation flux and corresponding column density at Ganymede within these bounds, $\sim 10^{13}$ H$_2$O cm^{-2} s^{-1} and $\sim 6 \times 10^{15}$ H$_2$O cm^{-2}, respectively. More recently, Vorburger et al. ([2021](#)) attained a peak number density of $\sim 4 \times 10^9$ cm^{-3}. Thus, the constraints we estimated for H$_2$O are similar to what has been suggested at Europa and are within the broad range suggested at Ganymede, contrary to previous models that assumed more H$_2$O in Callisto's atmosphere.

4.2. Radiolytically Produced H$_2$

Since, as described above, the morphology of H is similar to that of its parent species, the HST/STIS observation of an H corona at Callisto indicates a global source is required. As suggested in CM21, we confirm that a globally distributed H$_2$ component, in an atmosphere also containing H$_2$O and O$_2$, can qualitatively and quantitatively account for the observed H corona. Ignoring any ionospheric source, which is discussed below, the estimated average surface densities required to reproduce the observation are $n_{0,H_2} \sim 10^8$ cm^{-3} when hot H is solely produced via interactions with photons or $n_{0,H_2} \sim 4 \times 10^7$ cm^{-3} when hot H is also produced via interactions with magnetospheric electrons using our simple estimate for the flux.

As in CM20 and CM21, we assume that the near-surface density of H$_2$, primarily produced via radiolysis, is essentially global as it is efficiently redistributed and permeates the porous regolith from which it thermally reenters the atmosphere. Therefore, ignoring production in the atmosphere but accounting for dissociation and ionization, the simulated steady-state escape rate is indicative of the average production rate of H$_2$. In an H$_2$ + H atmosphere, this varies from $\sim (1.3–2.3) \times 10^{28}$ s^{-1} (corresponding to $\sim 47–84$ kg/s). When the O$_2$ component assumed here ($n_{0,O_2} \sim 10^9$ cm^{-3}; e.g., Figure [11](#)) and the H$_2$O component based on our constraints are included, they affect the H$_2$ component and the H it produces, thereby reducing this range by about half to $\sim (0.7–1.4) \times 10^{28}$ s^{-1} (corresponding to $\sim 26–51$ kg/s). The density of O$_2$ has been suggested to be larger than that considered here (e.g., Kliore et al., [2002](#)), and collisions with such a dense O$_2$ component would further reduce the H$_2$ escape rate. In addition, although absorption of reflected Lyman-α by O$_2$ is likely negligible (e.g., Roth et al., [2017b](#), Figure [2](#) therein), incoming photons could be absorbed by such a dense O$_2$ as we showed for H$_2$ (Figure [7](#)), further affecting H production.
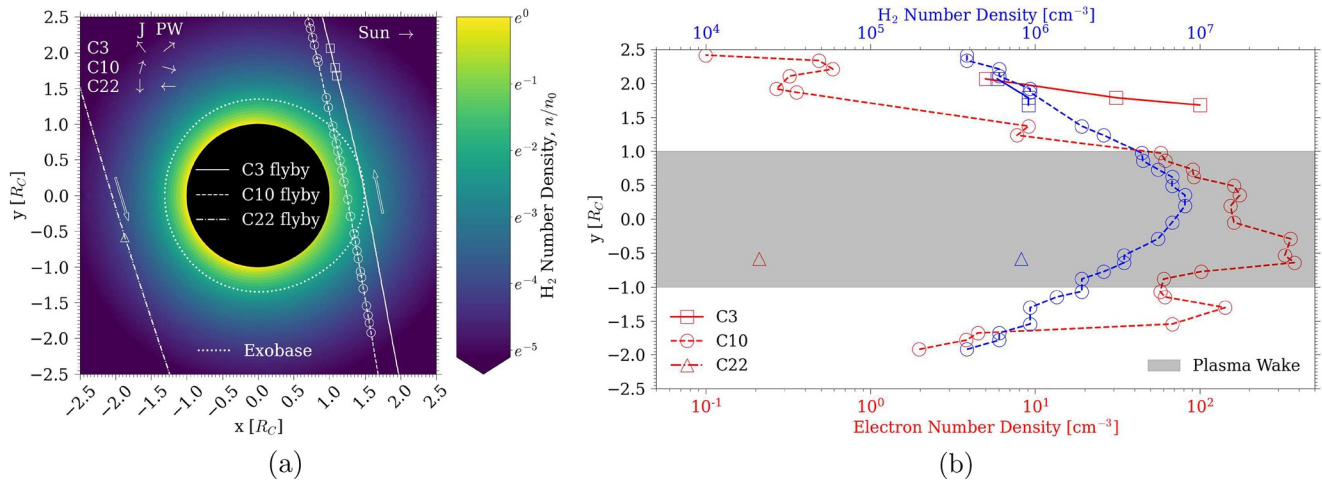
Figure 12. (a) The C3 (solid line), C10 (dashed line), and C22 (dash-dotted line) flyby trajectories are superimposed onto the H_2 density profile where $n_{0,H_2} \sim 4 \times 10^7$ cm^{-3}, interactions with photons and magnetospheric electrons are considered as given in Table B1, and an O_2 component with $n_{0,O_2} \sim 10^9$ cm^{-3} is also present. In this Callisto-centered x–y coordinate system, the Sun is located to the right (positive x-direction); the points at which electron densities were observed are denoted by white squares, circles, and a triangle for the C3, C10, and C22 flybys, respectively; the exobase is represented by the dotted white line; and arrows illustrating the direction *Galileo* flew by Callisto on the left (C22) and right (C3, C10) of the plot, as well as the general direction of Jupiter ("J") and the plasma wake ("PW") during these flybys in the upper left of the plot. (b) The electron densities (red lines; x-axis, *bottom*) observed during the C3, C10, and C22 flybys compared to the corresponding simulated H_2 densities (blue lines; x-axis, *top*) along the y-axis from (a). The shaded region roughly approximates the plasma wake region during all three flybys.

Consistent with CM21, H_2 escape rates do not linearly scale with n_{0,H_2} due to the influence of $H_2 + H_2$ collisions. The production and corresponding density of H exhibit a similar trend due to the influence of $H_2 + H$ collisions: the more collisional the H_2 component, the more the H density profile is enhanced (e.g., Figure 6). This issue becomes even more complicated when other collisional components are included (e.g., a dense, near-surface O_2 component) because, as discussed earlier, they can affect the spatial distribution of H_2, which in turn affects the H produced.

While we determined that a direct surface source of H cannot account for the observed corona (Section 3.3), there are *indirect* sources that we did not consider, which are outside the scope of this study. For example, below the H_2 exobase ionization can produce H_2^+, which in turn can collide with a neutral H_2 producing H_3^+ and a neutral H ($H_2^+ + H_2 \rightarrow H_3^+ + H$), and on recombination H_3^+ can subsequently produce even more H ($H_3^+ + e \rightarrow H + H + H$) as well as recycle neutral H_2 ($H_3^+ + e \rightarrow H_2 + H$). These additional sources of energized H could reduce the required n_{0,H_2} to produce the observed H corona and the concomitant H_2 escape rates. However, as the H_2 atmosphere thins out due to the reduced surface density, then the $H_2 + H$ collisions will be less efficient at enhancing the H density via collisions. In addition, as the surface density decreases, so too do the H_2 exobase altitudes until the atmosphere is dominated by O_2 (e.g., CM21). When this is the case the ionosphere would be dominated by interactions with O_2, thereby limiting the contribution to the H corona and the H_2 escape rate. Thus, the decrease in H_2 density cannot be too much so that the H_2 exobase is still well above the other collisional components in Callisto's atmosphere. A self-consistent hybrid model combining the atmosphere, the ionosphere, and the surrounding plasma is required to investigate these interactions.

4.3. *Galileo* Plasma-Wave Observations

Gurnett et al. (1997) suggested that an extended atmospheric component was likely responsible for the enhanced electron densities observed by *Galileo*'s plasma-wave instrument as the spacecraft crossed into the plasma sheet during the C3 flyby (e.g., Figure 12a). Since the observed electron densities at the relevant altitudes were orders of magnitude larger than the background magnetospheric electron density (cf., Figure 12b and Table D2 in Appendix D), they suggested it was produced by the ionization of a neutral gas implying "a significant neutral

atmosphere must exist around Callisto." They also suggested it might be related to the atomic hydrogen cloud detected at Ganymede (Barth et al., 1997; Feldman et al., 2000). Since the C/A of this flyby, at 1,129 km ($1.47R_C$), is well above the altitudes of the presumably O_2-sourced ionospheric component deduced from the radio-wave deflections ($\lesssim 50$ km; Kliore et al., 2002), an extended source is required, which we suggest is H_2. The subsequent flybys provided little clarity on the composition and spatial distribution of the suggested atmosphere (Gurnett et al., 2000). Whereas the C22 flyby, with a C/A altitude of 2,299 km ($1.95R_C$), resulted in a maximum electron density of only ~ 0.21 cm^{-3} near C/A in the wake region, the C10 flyby with a C/A altitude of 535 km ($1.22R_C$) confirmed the presence of a highly extended, enhanced component with peak densities orders of magnitude larger than that of the background Jovian magnetosphere plasma density at Callisto's orbit (cf., Figure 12b and Table D2 in Appendix D). Since relatively high plasma densities were measured within altitudes of 535 km (C10 flyby) and 1,129 km (C3 flyby) but not at an altitude of 2,299 km (C22 flyby), Gurnett et al. (2000) suggested that the observations were indicative of a high-altitude ionospheric distribution. In addition, as the C3 and C10 flybys occurred on the day-side but the C22 flyby occurred on the night-side (Figure 12a), they suggested its production was due to solar illumination.

Using a hybrid plasma model to describe the energetic plasma flow during the C10 flyby, Liuzzo et al. (2016) considered only O_2 and CO_2 components and, as a result, required even larger neutral densities than those inferred by Carlson (1999) and Kliore et al. (2002) to account for the plasma-wave observations. Because the densities of these components, as well as that of H_2O, are negligible at the relevant altitudes of the aforementioned flybys, and the local H density is much less than that of the H_2, we propose that the inferred electron densities, n_e, were determined by the local density of H_2, its ionization rate, and the electron loss rate. In Figure 12a, we superimposed the C3, C10, and C22 trajectories onto the H_2 density profile for the case in which $n_{0,H_2} \sim 4 \times 10^{-7}$ cm^{-3} in a multicomponent atmosphere and interactions with both photons and magnetospheric electrons lead to ionization. The observation represented by circles, squares, and a triangle along the spacecraft trajectories are all very close to Callisto's orbital plane ($<5°$ latitude) throughout the flybys with C/A ranging from 594 to 2,299 km (1.22–$1.95R_C$), and the direction of the spacecraft motion as well the plasma wake are indicated by arrows. The three trajectories are seen to sample a drop-off of only a few H_2 scale heights, and several of the C10 measurements are taken below the H_2 exobase, suggesting the extended ionospheric processes described in Section 4.2 could occur. Here, we define the exobase at the altitudes where the Knudsen number, Kn $= \ell/H \sim 1$, with ℓ and H the local mean free path and scale height of H_2, respectively.

Assuming the electrons produced from H_2 are primarily picked up and swept out of the region by the rapidly rotating Jovian field in a time τ_e, then n_e is roughly proportional to n_{H2}

$$n_{H_2} \Sigma_i \left(\nu_{pe} + \nu_{h\nu} \right) \sim n_e/\tau_e \qquad (6)$$

The data points for n_e and n_{H_2} are represented in red and blue in Figure 12b, respectively; and i indicates the sum over the ionizing processes induced via interactions with plasma electrons (pe) and photons (hν) in Table B1 in Appendix B with a net ionization rate $\nu_{pe} + \nu_{h\nu} \sim 7.4 \times 10^{-8}$ s^{-1}. As will be discussed below, ν_{pe} and τ_e can be highly variable, which would have a relatively small effect on the H_2 density profile, but a significant effect on the electron production rate. Assuming the net ionization rate is fixed, then from Figure 12b τ_e would be roughly proportional to n_e/n_{H_2}, and varies from $\sim 10°$–10^3 s. The shorter times are consistent with loss by pickup and sweeping, which for a distance of R_C is $\sim 10^1$ s. The longer times in the more depleted regions are comparable to average half bounce times (the time an electron travels from Callisto to its mirror point and back), $\gtrsim 10^2$ s for 100 eV electrons (e.g., Liuzzo et al., 2019, Figure 2a therein), suggesting the assumption of a uniform irradiation by the plasma electrons is a rough approximation.

In Figure 12b, it is seen for C10 that as *Galileo* crosses the plasma wake region, the electron density very roughly scales with the H_2 density allowing for the expected plasma turbulence in the wake. Because our 2D model is axisymmetric about the line passing through the subsolar point, but the plasma flow is not, the differences in the profiles on either side of the wake are not surprising. As the ion gyroradii are on the order of or larger than Callisto's radius (Cooper et al., 2001, Figure 4 therein) and the magnetic field points downward, enhanced plasma densities prior to entering the wake and depleted densities on exiting are expected.

Table 2
Callisto's Neutral H_2 Torus

	Upper estimate (a)	Lower estimate (b)
H_2 surface density, n_0 [($\times 10^8$) cm^{-3}]	1.0	0.4
Escape rate, Φ_{esc} [($\times 10^{28}$) s^{-1}]	1.4	0.68
Escape speed, v_{esc} (c) 10 [km s^{-1}]	0.90	1.1
Lifetime, τ [t_{orb}]	78 (d)	8.4 (e)
Radial extent, ΔR_{torus} (f) [R_J]	12	14
Scale height, H_{torus} (g) [R_J]	1.4	1.8
Average torus density, n_{torus} (h) [($\times 10^2$) cm^{-3}]	3.9	0.14
Average density at Hill sphere, $n_{H_2}(r_{HS})$ [($\times 10^2$) cm^{-3}]	9.8	4.4

[a]Simulation results where only interactions with photons are considered and an O_2 component with $n_{0,O_2} \sim 109$ cm^{-3} is present. [b]Simulation results where interactions with photons and an upper limit for magnetospheric electrons are considered and an O_2 component with $n_{0,O_2} \sim 10^9$ cm^{-3} is present. [c]For reference, the escape speed from Jupiter at d_{JC} is $\sqrt{2GM_J/(R_J + d_{JC})} \sim 11.4$ km/s and the speed required to reach Callisto's Hill sphere from the surface is $\sqrt{2GM_C(1/R_C - 1/r_{HS})} \sim 2.39$ km/s. Here, $G = 6.674 \times 10^{-11}$ m^3 kg^{-1} s^{-2} is the gravitational constant and $M_C = 1.076 \times 10^{23}$ kg and $M_J = 1.898 \times 10^{27}$ kg are the masses of Callisto and Jupiter, respectively. [d]$\tau = 1/(\Sigma_i \nu_{i,photons})$, where i represents the number of photochemical reactions considered and $\nu_{photons}$ are the corresponding reaction rates from Table B1 in Appendix B scaled to an "average" Sun (Huebner & Mukherjee, 2015; i.e., with solar activity = 0.5 from https://phidrates.space.swri.edu/ and rates scaled to 5.2 AU). [e]$\tau = 1/((\Sigma_i \nu_{i,photons}) + (\Sigma_j \nu_{j,electrons}))$, where j represents the number of magnetospheric electron-impact-induced reactions considered and $\nu_{electrons}$ are the corresponding reaction rates from Table B1 in Appendix B. [f]$\Delta R_{torus} = d_{JC}(4v_{esc}/v_C)$ (Johnson, 1990). [g]$H_{torus} = d_{JC}(v_{esc}/2v_C)$ (Johnson, 1990). [h]$n_{torus} = \Phi_{esc}\tau/V_{torus}$ (Johnson, 1990), where $V_{torus} = 2\pi d_{JC}(2\Delta R_{torus})(2H_{torus})$ is the volume of the torus.

The observed electron densities for C10 differs from that for C22 in a similar region by about 3 orders of magnitude. Whereas the latter occurred near western elongation $4.31R_J$ below the plasma sheet and in Callisto's shadow, the former occurred near eastern elongation $2.45R_J$ below the plasma sheet and exposed to the Sun (Seufert, 2012), which could contribute to the differences in observed electron densities. Contrary to this comparison, although the three measurements taken during the C3 flyby also very roughly scale with the H_2 density like those during the C10 flyby in a similar region, the electron densities for the former are about 1–2 orders of magnitude larger than those for the latter. Interestingly, the C3 flyby occurs when Callisto was farther from the plasma sheet, $3.24R_J$ and above it (Seufert, 2012). Since both observations occur on the day-side with Callisto near eastern elongation and the average solar irradiance only varied by $\lesssim 10\%$ (e.g., Schmutz, 2021, Figure 2 therein) in the 3-years interval between them, this comparison suggests that the plasma induced ionization dominates the difference in electron production. Indeed, as shown in Table D2 in Appendix D, the background plasma density was larger during the C3 flyby than that during the C10 flyby, with a temperature more efficient for ionization (e.g., Straub et al., 1996).

Since the C22 flyby occurred over the night-side of Callisto and the C3 and C10 flybys occurred over the day-side, photoionization could be a required source for the extended ionosphere and/or it could be a transient phenomena, varying temporally as well as spatially. Since the Jovian magnetodisk wobbles relative to Callisto's orbital plane by $\sim 10°$ and, as a result, Callisto moves in and out of the Jovian plasma sheet, it experiences magnetic distances between $\sim 26R_J(d_{JC})$ and as large as $\sim 70R_J$ ($\sim 2.7d_{JC}$) (Paranicas et al., 2018, Figure 2 therein), resulting in a highly variable plasma environment. Thus, a detailed model is needed to determine the highly variable source and loss rates in an extended H_2 atmosphere as Callisto moves in and out of the plasma sheet. Nevertheless, based on our results for a global H_2 atmosphere and the similar profiles illustrated in Figure 12b, we suggest that these observations are consistent with an extended H_2 atmosphere.

4.4. Neutral H_2 Torus

Since the H_2 that escapes from Callisto does not escape from the Jovian system and has a lifetime longer than Callisto's orbital period (Table 2), a yet to be detected neutral H_2 torus will form (e.g., CM21). Using our simu-

lation results for steady-state H_2 escape rates (Φ) and speeds (v_{esc}) as well as the corresponding lifetimes (τ), we very roughly estimate the average torus density (n_{torus}) corotating with Callisto using the analytical estimate from Johnson (1990) in Table 2. We also include the H_2 densities at Callisto's Hill sphere, $r_{HS} \sim 0.7R_J$, which is a rough upper bound for the peak densities in the torus.

The lifetime, τ, is estimated using average plasma parameters at Callisto's orbit, even though molecules with significant eccentricities experience a large range of plasma parameters. For example, the rough estimate for the radial extent, $\Delta R_{torus} \sim 12 - -14R_J$ (Table 2), implies that H_2 from Callisto could reach Ganymede's orbit ($\sim 15R_J$), where the plasma densities are significantly larger, reducing τ, as well as making it difficult to distinguish the sources. However, based on the rough estimate of the scale height, $H_{torus} \sim 1.4 - -1.8R_J$ (Table 2), n_{torus} will have dropped off several orders of magnitude prior to reaching Ganymede's orbit. With much faster average escape speeds, $v_{esc} \sim 12$–16 km/s, and much smaller escape rates, $\Phi \sim (1.0$–$1.5) \times 10^{26}\,s^{-1}$, any H component in the Callisto torus will be orders of magnitude smaller than that estimated for H_2.

Using our lowest estimate of $n_{torus} \sim 14\,cm^{-3}$ (Table 2), Callisto's average H_2 torus density is on the order of Europa's neutral torus: Lagg et al. (2003) and Mauk et al. (2003) inferred average H_2 torus densities at Europa of ~ 20–25 and $\sim 40\,cm^{-3}$, respectively; Smyth and Marconi (2006) reported an average H_2 torus density at Europa of $\sim 90\,cm^{-3}$; and Smith et al. (2019) reported an average neutral torus density of $\sim 27\,cm^{-3}$ for all species, but H_2 accounted for most of the particles in this estimate. Kollmann et al. (2016) analyzed *Galileo* Energetic Particles Detector (EPD) data at Europa's orbit over a range of magnetic latitudes to constrain the thickness of the local torus. Although results from their analysis were consistent with those of Lagg et al. (2003), since the source rate of energetic particles near Europa's orbit is not well known, they could only make a relatively broad constraint for equatorial H_2 of ~ 1–$410\,cm^{-3}$. From recent Juno observations, Szalay et al. (2022) confirmed the presence of a Europa-genic neutral H_2 toroidal cloud, which is expected to be the primary cloud constituent (Smith et al., 2019). However, since they were derived from H_2^+ pickup ion densities, they refrained from estimating the concomitant neutral H_2 densities in the toroidal cloud, and suggested more complex modeling is required to do so. The simulated H_2 neutral loss rates from Callisto presented here (Section 4.2) are larger than those derived for Europa by Szalay et al. (2022). Moreover, since the neutral lifetimes are much shorter at Europa (Oza et al., 2019), its toroidal cloud's spatial extent is more confined than at Callisto. Thus, a larger H_2 neutral toroidal cloud could form around Callisto, albeit a more detailed comparison is required.

5. Conclusion

We simulated Callisto's thin atmosphere in 2D using the DSMC method (Bird, 1994) to determine the source of the H corona observed by HST/STIS at eastern elongation (Roth et al., 2017a). Our results showed that H_2O is not the dominant source of H and that a roughly global extended source is required. Noting the presence of a near-surface atmosphere dominated by radiolytically produced O_2, we show that the source of the H corona is consistent with the concomitant H_2 atmospheric component. This global H_2 atmosphere can also account for the electron densities observed by *Galileo*'s plasma-wave instrument (Gurnett et al., 1997, 2000). Thus, we present the first evidence of H_2 in Callisto's atmosphere.

An upper limit to the H_2 surface source rate was determined when only interactions with photons are considered as sources of H, but a more realistic source rate was shown to depend strongly on the uncertain production of H by the magnetospheric electrons penetrating the extended H_2 atmosphere. It also depends on the not well constrained near-surface O_2 component and the ionosphere it can produce, the former can inhibit H_2 escape via collisions and the latter can affect the magnetospheric electron flux (e.g., Strobel et al., 2002). Consistent with CM21, the reduction in steady-state escape rate does not scale linearly with the corresponding reduction in the H_2 surface density, which varied by a factor of 2.5 for the cases discussed, from $\sim 10^8\,cm^{-3}$ to $\sim 4 \times 10^7\,cm^{-3}$. These values were ~ 10–$25\times$ less than that we assumed for O_2: $\sim 10^9\,cm^{-3}$, which produces a disk-averaged column density of $\sim 5 \times 10^{15}\,cm^{-2}$ (Figure 11b), consistent with that suggested by Cunningham et al. (2015) $3.4^{+2.0}_{-1.8} \times 10^{15}\,cm^{-2}$.

Simulations of the production of H from sublimated H_2O for two significantly different models of the surface ice were considered in which the ice and dark nonice or ice-poor material are intimately mixed or segregated into patches. Neither scenario reproduces the observed morphology of the H corona. Based on the often used "IM" model the peak H_2O number density is constrained to $\lesssim 10^8$ cm^{-3}, indicating that previous models of Callisto's atmosphere overestimated the amount of gas-phase H_2O by 1–2 orders of magnitude. Our simulation results place upper limits on peak H_2O production and density in Callisto's atmosphere, but cannot distinguish which of the two sublimation scenarios we considered is more likely—something that forthcoming spacecraft observations can distinguish. However, based on the visual evidence (e.g., Moore et al., 1999; Spencer, 1987b; Spencer & Maloney, 1984), we suggest that H_2O sublimation at Callisto is more likely to occur in a manner similar to that described by the "SP" scenario. Other possible direct sources for the H were considered, such as proton charge-exchange and direct sputtering of H, but are insufficient to reproduce the observation.

Although no neutral torus has yet been detected at Callisto's orbit, based on the range of H_2 escape rates, escape speeds, and estimated lifetimes, a range of approximate average densities of the neutral H_2 torus corotating with Callisto is given. Comparing source rates to those estimated at Ganymede (Leblanc et al., 2017; Marconi, 2007) and Europa (Szalay et al., 2022 and references therein), in combination with longer local lifetimes, a potentially detectable H_2 torus could form around Callisto. Further, the constraints we estimated for H_2O sublimation fluxes are similar to what has been suggested at Europa and are within the broad range suggested at Ganymede, contrary to previous models that assumed much larger fluxes at Callisto. The results presented here also suggest that the role of H_2 versus H_2O as a source of an H corona should be reexamined at Europa (e.g., Roth et al., 2017b) and Ganymede (e.g., Alday et al., 2017; Barth et al., 1997; Feldman et al., 2000) since their morphologies were similar to that at Callisto but the primary source of the H was assumed to be sublimated H_2O. The possibility of H_2 being the primary source of their H coronae can affect our understanding of the weathering of their icy surfaces and production of their atmospheres.

Future work is needed to examine reactions in the regolith, the neutral atmosphere, and the ionosphere to determine how much H_2 comes from water ice and from hydrocarbons and hydrated minerals in the dark nonice surface materials, as well as to better constrain the O_2 component in Callisto's atmosphere. DSMC simulations, similar to those presented here, can be used to determine how much O_2 is required to reproduce the observed O corona (Cunningham et al., 2015) as well as any contribution from H_2O (e.g., Roth et al., 2021), thereby better constraining their source rates and surface densities. More important, a self-consistent model coupling Callisto's atmosphere and ionosphere to the local plasma environment is needed to account for the possible ionospheric sources of H described in Section 4.2.

Herein we have shown that in a four component (H_2O, H_2, O_2, H) collisional atmosphere at Callisto subject to interactions with solar photons and magnetospheric electrons the morphology of the observed H is reproduced primarily via dissociation of H_2 with an average surface density of $n_{0,H_2} \sim 4 \times 10^7$ cm^{-3}, with a minor contribution of H from sublimated H_2O with a peak number density $\lesssim 10^8$ cm^{-3} (Figures 10 and 11). The principal findings of this study—the first evidence of an appreciable H_2 component and constraints on the sublimation of H_2O in Callisto's enigmatic atmosphere—are exciting as they have implications for other icy satellites, lead to suggestions for possible spacecraft confirmation, and open the door for several new studies going forward.

Appendix A: DSMC and LOS Grids

Figures A1 and A2 illustrate the Direct Simulation Monte Carlo (DSMC) and line-of-sight (LOS) grids implemented in this study.
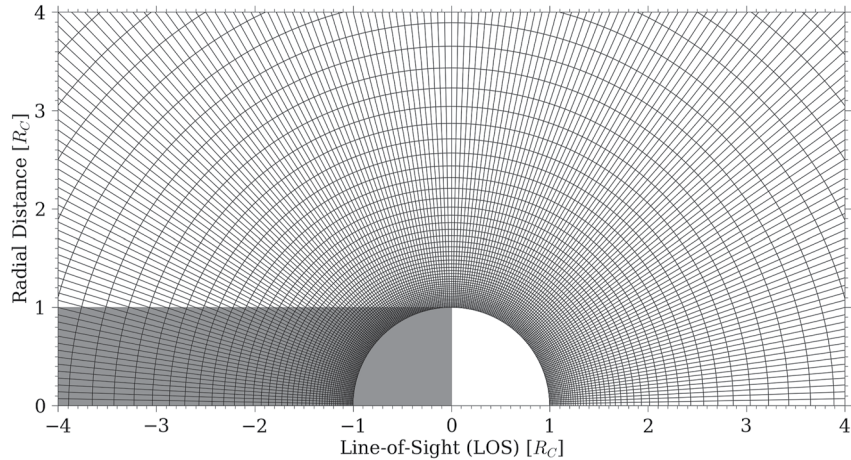
Figure A1. Example of a 2D Direct Simulation Monte Carlo (DSMC) grid used here. The lower and upper boundaries of the radial cells are set to Callisto's surface, $r_0 = R_C = 2{,}410$ km, and the Hill sphere, $r_{max} \sim 20.8 R_C$ ($r_{max} - r_0 \sim 48{,}000$ km), respectively. We refer the reader to CM21 (Appendix B therein) for how the extent of radial cells are determined. The subsolar latitude (SSL) axis extends from the subsolar point (SSL $= 0°$) to the antisolar point (SSL $= 180°$) with uniform angular increments ΔSSL $= 1°$, and the domain is symmetric about the axis passing through these points. The x-axis of this figure represents the LOS from the Sun to Callisto, and extends from $-r_{max} \rightarrow +r_{max}$, where positive and negative values represent the foreground and background of Callisto, respectively, with the center of Callisto at $x = 0$. The y-axis of this figure is the radial distance perpendicular to the LOS, and extends from $0 \rightarrow r_{max}$, with the center of Callisto at $y = 0$. The Sun is located to the right of the figure (positive x-axis). The shaded region on and off the disk represents the night-side and Callisto's shadow, respectively.
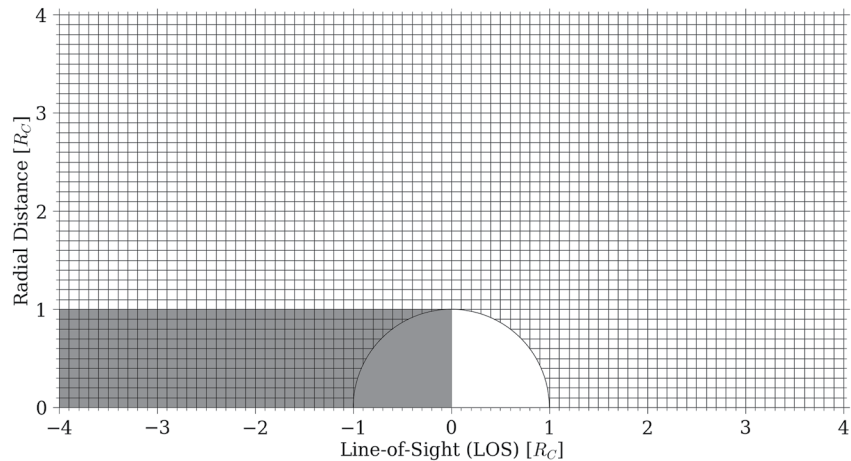

Figure A2. The 2D line-of-sight (LOS) grid used here to calculate H LOS column densities (Figures 4–6 and 8–10) and photoabsorption due to opacity (Figure 7). The x-axis of this figure represents the LOS from the Sun to Callisto, and extends from $-r_{max} \rightarrow +r_{max}$, where positive and negative values represent the foreground and background of Callisto, respectively, with the center of Callisto at $x = 0$. The y-axis of this figure is the radial distance perpendicular to the LOS, and extends from $0 \rightarrow r_{max}$, with the center of Callisto at $y = 0$. The increments for both axes are $0.1 R_C$. A particle, p, is located within a certain cell if $r_p \cos(\text{SSL}_p)$ and $r_p \sin(\text{SSL}_p)$ are within the cell's bounds along the x-axis and y-axis, respectively. The Sun is located to the right of the figure (positive x-axis). The shaded region on and off the disk represents the night-side and Callisto's shadow, respectively.

Appendix B: Photochemical and Electron-Impact-Induced Reaction Rates

Table B1 lists the various reactions considered in Callisto's atmosphere in this study.

Table B1

Dissociation, Ionization, and Dissociative Ionization Rates via Interactions With Photons and Magnetospheric Electrons in Callisto's Atmosphere

Reaction		Rate [s^{-1}]	Excess energy [eV]
(1)	$H_2O + h\nu \rightarrow H + OH$	6.51×10^{-7}	4.04
(2)	$H_2O + h\nu \rightarrow H + H + O$	7.06×10^{-8}	0.697
(3)	$H_2O + h\nu \rightarrow H_2 + O$	5.47×10^{-8}	3.94
(4)	$H_2O + h\nu \rightarrow H_2O^+ + e$	3.06×10^{-8}	15.2
(5)	$H_2O + h\nu \rightarrow H + OH^+ + e$	5.58×10^{-9}	23.2
(6)	$H_2O + h\nu \rightarrow OH + H^+ + e$	1.50×10^{-9}	30.5
(7)	$H_2O + h\nu \rightarrow H_2 + O^+ + e$	8.17×10^{-10}	39.8
(8)	$H_2 + h\nu \rightarrow H_2^+ + e$	4.25×10^{-9}	7.17
(9)	$H_2 + h\nu \rightarrow H + H$	4.03×10^{-9}	8.22
(10)	$H_2 + h\nu \rightarrow H + H^*$	3.04×10^{-9}	0.488
(11)	$H_2 + h\nu \rightarrow H + H^+ + e$	1.03×10^{-9}	27.0
(12)	$H_2O + e \rightarrow H + OH + e$	1.51×10^{-7}	4.04
(13)	$H_2O + e \rightarrow H_2O^+ + 2e$	9.65×10^{-8}	15.2
(14)	$H_2O + e \rightarrow H + OH^+ + 2e$	3.08×10^{-8}	23.2
(15)	$H_2O + e \rightarrow OH + H^+ + 2e$	2.65×10^{-8}	30.5
(16)	$H_2O + e \rightarrow H + H + O + e$	1.10×10^{-9}	0.697
(17)	$H_2 + e \rightarrow H_2^+ + 2e$	6.38×10^{-8}	7.17
(18)	$H_2 + e \rightarrow H + H + e$	1.29×10^{-8}	0.488
(19)	$H_2 + e \rightarrow H + H^+ + 2e$	5.88×10^{-9}	27.0

Note. Reactions 1–11: From Huebner and Mukherjee (2015) for an "active" Sun (i.e., assuming solar maximum) and scaled to 5.2 AU, ignoring possible absorption with depth into the atmosphere. The Sun was near solar maximum at the time of the original observation of Callisto from which the H corona was detected (Strobel et al., 2002), December 2001. Reactions 12–19: Assume the electron number density, n_e, and temperature, $k_B T_e$, derived from *Voyager* measurements by Neubauer (1998): $n_e = 1.1$ cm^{-3} and $k_B T_e = 100$ eV. Reactions 12–17, 19: Assume same excess energies as analogous photochemical reactions. Reaction 18: Excess energy from Reaction 10 (e.g., Tseng et al., 2013; see discussion in Section 2.3.2). Reaction 12: Rate based on cross-section data from Harb et al. (2001). Reactions 13–15: Rates based on cross-section data from Itikawa and Mason (2005). Reaction 16: Rate based on cross-section data from Kedzierski et al. (1998). Reaction 18: Rate based on cross-section data from Scarlett et al. (2018). Reactions 17 and 19: Rates based on cross-section data from Straub et al. (1996).

Appendix C: Temperature-Dependent Residence Time for H$_2$O

The binding energy and lattice vibration frequency of H$_2$O used to derive Δt_{res} are taken from ice-related experiments (Sandford & Allamandola, 1988, 1990), but are used here for H$_2$O molecules on Callisto's nonice or ice-poor surface material. This same implementation of applying Δt_{res} for H$_2$O molecules landing on nonice material has been done at the Moon for H$_2$O hopping away from cold traps and desorbing from Lunar regolith (Stewart et al., 2011). Thus, although simulating the ensuing processes which occur after H$_2$O molecules return to the nonice or ice-poor patches can be improved in the future, this approach is reasonable for a first-order approximation as has been similarly applied in the literature. Finally, since these DSMC simulations can be run for several Callisto orbital periods, $t_{orb} = 1.44 \times 10^6$ s, to reduce statistical noise, if $\Delta t_{res} > t_{orb}$ then the particle is removed from the simulation. Removing these particles has a negligible effect on the overall distribution since relatively few particles migrate to such regions of the surface where $\Delta t_{res} > t_{orb}$. Moreover, consistent with CM21, steady-state for the SP-Ice Return simulations is reached in a fraction of t_{orb} (Figure C1).
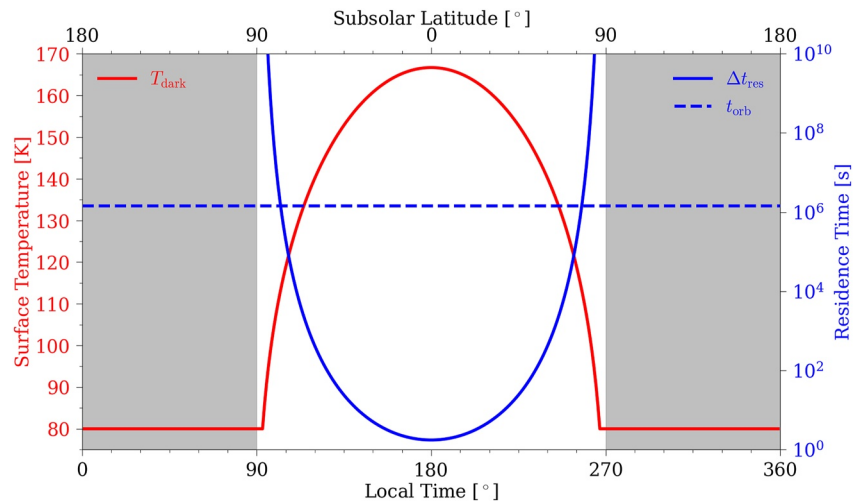
Figure C1. Temperature-dependent residence time for H_2O molecules on the nonice or ice-poor material, Δt_{res} (solid blue line, right y-axis) as a function of the corresponding temperature distribution, T_{dark}(SSL) (solid red line, left y-axis), in the segregated patches scenario. For reference we also include Callisto's orbital period, $t_{orb} = 1.44 \times 10^6$ s (dashed blue line). The gray background represents the night-side.

Appendix D: Callisto's Physical and Local Plasma Parameters

Tables D1–D4 lists various physical parameters of Callisto as well as of the local plasma.

Table D1
Various Physical Parameters of Callisto

Physical parameters [units]	
Radius, R_C [km]	2,410
Mass, M_C [kg]	1.08×10^{23}
Distance from Jupiter, d_{JC} [R_J[a]]	26.3
(Average) distance from Sun [AU]	5.20
Hill sphere, r_{HS}[b] [R_C (R_J)]	20.8 (0.701)
Orbital period, t_{orb} [s (days)]	1.44×10^6 (16.7)
Orbital velocity, v_C [km s^{-1}]	8.20

[a]R_J = 71, 492 km is the radius of Jupiter. [b]$r_{HS} = \left(\frac{M_C}{3M_J} \right)^{1/3} d_{JC}$, where $M_J = 1.898 \times 10^{27}$ kg is the mass of Jupiter.

Table D2
Background Plasma Density and Ion Temperature Estimates Taken From Tables 3.1 and 3.2 in Seufert (2012) for Galileo C3, C10, and C22 Flybys

Flyby	Distance from plasma sheet[a] [R_J]	Background plasma density [cm^{-3}]	Ion temperature[b] [eV]
C3	3.24	0.12	111
C10	−2.45	0.04	964
C22	−4.31	0.03	1,030

[a]Positive and negative values indicate Callisto was above and below the plasma sheet, respectively. [b]Ion temperature in the background plasma will be comparable to that of the electrons.

Table D3

Proton Parameters Taken From Vorburger et al. (2019) and References Therein

Parameter [units]	Thermal	Energetic
Number density [cm^{-3}]	$(10^{-3}–10^{-1})$[a]	$(10^{-4}–10^{-2})$[a]
Temperature [keV]	0.2	20
Speed [km/s]	192[b]	3,910[c]

[a]Lower and upper bounds roughly represent minimum and maximum values of the local proton densities, respectively. [b]Average relative speed between the local plasma azimuthal velocity and Callisto's orbital velocity (Kivelson et al., 2004). [c]$\sqrt{8kT/\pi/m_{H+}}$, where $kT = 20$ keV.

Table D4

Temperature-Dependent Charge-Exchange Cross-Sections Taken From Rinaldi et al. (2011) and References Therein

Reaction	Temperature [keV]	Cross-section[a] ($\times 10^{16}$) [cm^2]
$H^+ + H \rightarrow H + H^+$	0.1–10	4–30
$H^+ + O \rightarrow H + O^+$	0.1–10	3.4–70
$H^+ + H_2 \rightarrow H + H_2^+$	0.1–10	0.3–10
$H^+ + O_2 \rightarrow H + O_2^+$	0.5–10	5.6–14
$H^+ + H_2O \rightarrow H + H_2O^+$	0.5–5	12.4–19.8
$H^+ + CO_2 \rightarrow H + CO_2^+$	0.1–10	7–16

[a]Upper and lower bounds represent minimum and maximum values estimated over the temperature range given, which are not necessarily related to the upper and lower bounds of the temperatures.

Appendix E: Wavelength-Dependent Photoabsorption Cross-Sections and Photochemical Reaction Rates

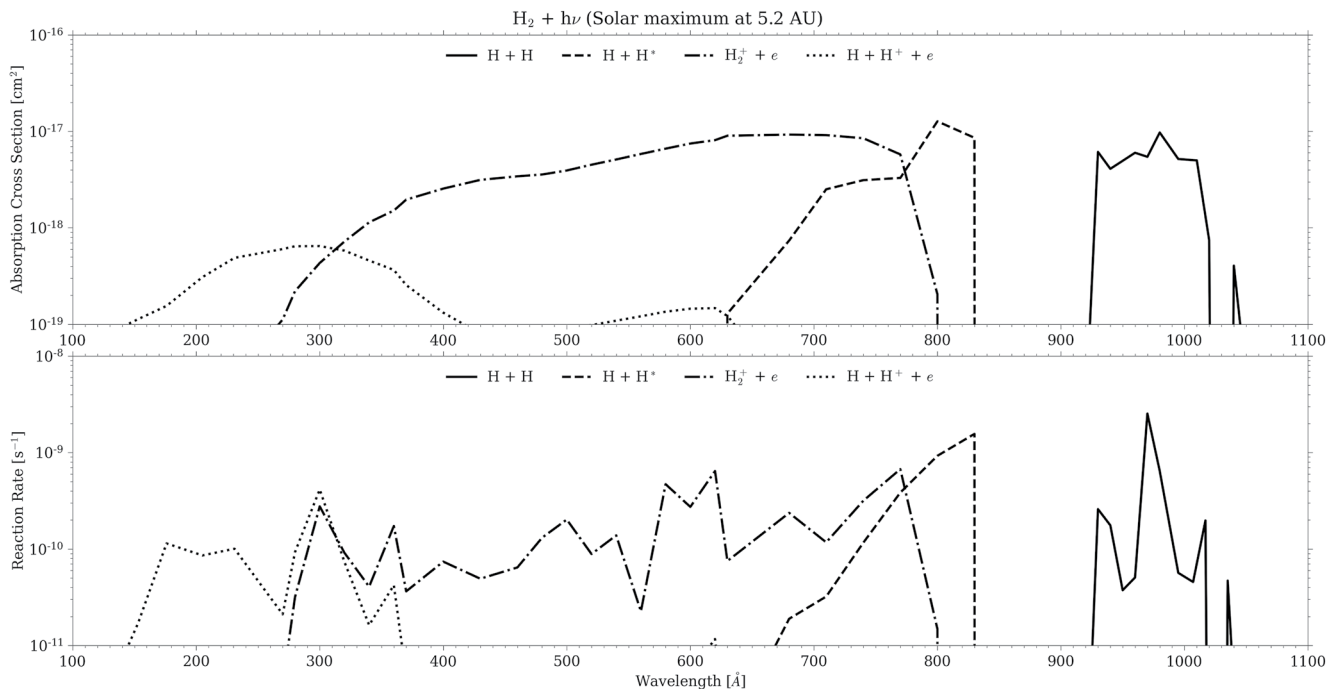Figure E1 illustrates wavelength-dependent photoabsorption cross-sections and photochemical reaction rates for H_2.

Figure E1. Photoabsorption cross-sections (top) and photochemical reaction rates (bottom) as a function of wavelength for H_2 assuming solar maximum (Huebner & Mukherjee, 2015; https://phidrates.space.swri.edu/) scaled to 5.2 AU.

Appendix F: Statistical Noise in DSMC Results

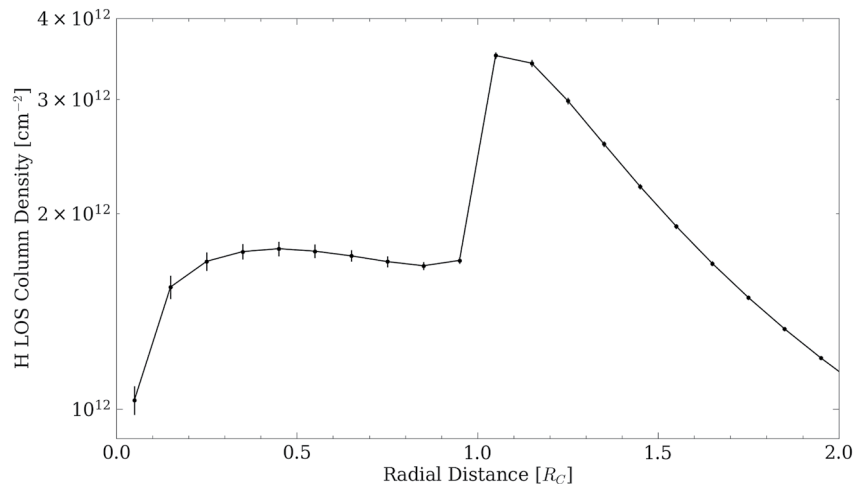Figure F1 illustrates the statistical noise inherent in DSMC results.

Figure F1. Steady-state result for H line-of-sight (LOS) column density in an H_2 + H atmosphere illustrated by a solid black line with the standard deviation between averaged values at each data point shown by small vertical black lines. The dip in LOS column density at the center of the disk is an artifact of using radial bins for the density simulations and azimuthal bins for the LOS estimate. After reaching steady-state, this simulation was run for an additional 10^6 time steps, with samples taken every 10^3 time steps and averages of those samples taken every 10^5 time steps. As can be seen, the largest uncertainty is over the disk, where the LOS bins are the smallest, and with increasing distance from the disk and increasing LOS bin size, the uncertainty diminishes. These small, negligible fluctuations in LOS column density over the disk do not affect the comparison of the corresponding coronal brightness to the HST data because the atmospheric signals overlap with the sunlight reflected from the surface, which dominates the local emissions (Section 3.3). As discussed in Section 2.4, off the disk, where these fluctuations are seen to be even smaller, the sunlight reflectance is negligible and the comparison to the HST data are the most reliable for constraining the H corona.

Data Availability Statement

The data used from the various models presented here to produce Figures 3–12 can be accessed from Carberry Mogan (2022).

References

Acharyya, K. (2014). Laboratory study of sticking and desorption of H_2 and its significance in the chemical evolution of dense interstellar medium. *Monthly Notices of the Royal Astronomical Society*, *443*(2), 1301–1309. https://doi.org/10.1093/mnras/stu1219

Acton, C., Bachman, N., Semenov, B., & Wright, E. (2018). A look towards the future in the handling of space science mission geometry. *Planetary and Space Science*, *150*, 9–12. https://doi.org/10.1016/j.pss.2017.02.013

Acton, C. H. (1996). Ancillary data services of NASA's navigation and ancillary information facility. *Planetary and Space Science*, *44*(1), 65–70. https://doi.org/10.1016/0032-0633(95)00107-7

Alday, J., Roth, L., Ivchenko, N., Retherford, K. D., Becker, T. M., Molyneux, P., & Saur, J. (2017). New constraints on Ganymede's hydrogen corona: Analysis of Lyman-α emissions observed by HST/STIS between 1998 and 2014. *Planetary and Space Science*, *148*, 35–44. https://doi.org/10.1016/j.pss.2017.10.006

Anderson, J. D., Lau, E. L., Sjogren, W. L., Schubert, G., & Moore, W. B. (1997). Gravitational evidence for an undifferentiated Callisto. *Nature*, *387*(6630), 264–266. https://doi.org/10.1038/387264a0

Barth, C. A., Hord, C. W., Stewart, A. I. F., Pryor, W. R., Simmons, K. E., McClintock, W. E., et al. (1997). Galileo ultraviolet spectrometer observations of atomic hydrogen in the atmosphere of Ganymede. *Geophysical Research Letters*, *24*(17), 2147–2150. https://doi.org/10.1029/97GL01927

Bird, G. A. (1994). *Molecular gas dynamics and the direct simulation of gas flows*. Clarendon Press.

Brinkmann, R. T. (1970). Departures from Jeans' escape rate for H and He in the Earth's atmosphere. *Planetary and Space Science*, *18*, 449–478. https://doi.org/10.1016/0032-0633(70)90124-8

Buratti, B. J. (1991). Ganymede and Callisto: Surface textural dichotomies and photometric analysis. *Icarus*, *92*(2), 312–323. https://doi.org/10.1016/0019-1035(91)90054-w

Calvin, W. M., & Clark, R. N. (1991). Modeling the reflectance spectrum of Callisto 0.25 to 4.1 µm. *Icarus*, *89*(2), 305–317. https://doi.org/10.1016/0019-1035(91)90180-2

Carberry Mogan, S. R. (2022). Data underlying the publication "Callisto's atmosphere: First evidence for H_2 and constraints on H_2O". https://doi.org/10.5061/dryad.mkkwh7132

Carberry Mogan, S. R., Tucker, O. J., & Johnson, R. E. (2021a). The influence of upper boundary conditions on molecular kinetic atmospheric escape simulations. *Planetary and Space Science*, *205*, 105302. https://doi.org/10.1016/j.pss.2021.105302

Carberry Mogan, S. R., Tucker, O. J., Johnson, R. E., Sreenivasan, K. R., & Kumar, S. (2020). The influence of collisions and thermal escape in Callisto's atmosphere. *Icarus*, *352*, 113932. https://doi.org/10.1016/j.icarus.2020.113932

Carberry Mogan, S. R., Tucker, O. J., Johnson, R. E., Vorburger, A., Galli, A., Marchand, B., et al. (2021b). A tenuous, collisional atmosphere on Callisto. *Icarus*, *368*, 114597. https://doi.org/10.1016/j.icarus.2021.114597

Carlson, R. W. (1999). A tenuous carbon dioxide atmosphere on Jupiter's moon Callisto. *Science*, *283*(5403), 820–821. https://doi.org/10.1126/science.283.5403.820

Cartwright, R. J., Nordheim, T. A., Cruikshank, D. P., Hand, K. P., Roser, J. E., Grundy, W. M., et al. (2020). Evidence for sulfur-bearing species on Callisto's leading hemisphere: Sourced from Jupiter's irregular satellites or Io? *The Astrophysical Journal Letters*, *902*(2), L38. https://doi.org/10.3847/2041-8213/abbdae

Chamberlain, J. W., & Hunten, D. M. (1987). *Theory of planetary atmospheres: An introduction to their physics and chemistry*. Academic Press.

Clark, R. N. (1980). Ganymede, Europa, Callisto, and Saturn's rings: Compositional analysis from reflectance spectroscopy. *Icarus*, *44*(2), 388–409. https://doi.org/10.1016/0019-1035(80)90033-0

Clark, R. N., & McCord, T. B. (1980). The Galilean satellites: New near-infrared spectral reflectance measurements (0.65–2.5 μm) and a 0.325–5 μm summary. *Icarus*, *41*(3), 323–339. https://doi.org/10.1016/0019-1035(80)90217-1

Cooper, J. F., Johnson, R. E., Mauk, B. H., Garrett, H. B., & Gehrels, N. (2001). Energetic ion and electron irradiation of the icy Galilean satellites. *Icarus*, *149*(1), 133–159. https://doi.org/10.1006/icar.2000.6498

Cunningham, N. J., Spencer, J. R., Feldman, P. D., Strobel, D. F., France, K., & Osterman, S. N. (2015). Detection of Callisto's oxygen atmosphere with the Hubble Space Telescope. *Icarus*, *254*, 178–189. https://doi.org/10.1016/j.icarus.2015.03.021

Feistel, R., & Wagner, W. (2007). Sublimation pressure and sublimation enthalpy of H_2O ice Ih between 0 and 273.16 K. *Geochimica et Cosmochimica Acta*, *71*(1), 36–45. https://doi.org/10.1016/j.gca.2006.08.034

Feldman, P. D., McGrath, M. A., Strobel, D. F., Moos, H. W., Retherford, K. D., & Wolven, B. C. (2000). HST/STIS ultraviolet imaging of polar aurora on Ganymede. *The Astrophysical Journal*, *535*(2), 1085. https://doi.org/10.1086/308889

Galli, A., Vorburger, A., Carberry Mogan, S. R., Roussos, E., Stenberg Wieser, G., Wurz, P., et al. (2022). Callisto's atmosphere and its space environment: Prospects for the Particle Environment Package on board JUICE. *Earth and Space Science*, *9*, e2021EA002172. https://doi.org/10.1029/2021EA002172

Grundy, W. M., Buie, M. W., Stansberry, J. A., Spencer, J. R., & Schmitt, B. (1999). Near-infrared spectra of icy outer solar system surfaces: Remote determination of H_2O ice temperatures. *Icarus*, *142*(2), 536–549. https://doi.org/10.1006/icar.1999.6216

Gurnett, D. A., Kurth, W. S., Roux, A., & Bolton, S. J. (1997). Absence of a magnetic-field signature in plasma-wave observations at Callisto. *Nature*, *387*(6630), 261–262. https://doi.org/10.1038/387261a0

Gurnett, D. A., Persoon, A. M., Kurth, W. S., Roux, A., & Bolton, S. J. (2000). Plasma densities in the vicinity of Callisto from Galileo plasma wave observations. *Geophysical Research Letters*, *27*(13), 1867–1870. https://doi.org/10.1029/2000GL003751

Hall, D. T., Strobel, D. F., Feldman, P. D., McGrath, M. A., & Weaver, H. A. (1995). Detection of an oxygen atmosphere on Jupiter's moon Europa. *Nature*, *373*(6516), 677–679. https://doi.org/10.1038/373677a0

Hanel, R., Conrath, B., Flasar, M., Herath, L., Kunde, V., Lowman, P., et al. (1979). Infrared observations of the Jovian system from Voyager 2. *Science*, *206*(4421), 952–956. https://doi.org/10.1126/science.206.4421.952

Harb, T., Kedzierski, W., & McConkey, J. (2001). Production of ground state OH following electron impact on H_2O. *The Journal of Chemical Physics*, *115*(12), 5507–5512. https://doi.org/10.1063/1.1397327

Hartkorn, O., Saur, J., & Strobel, D. F. (2017). Structure and density of Callisto's atmosphere from a fluid-kinetic model of its ionosphere: Comparison with Hubble Space Telescope and Galileo observations. *Icarus*, *282*, 237–259. https://doi.org/10.1016/j.icarus.2016.09.020

Huebner, W. F., & Mukherjee, J. (2015). Photoionization and photodissociation rates in solar and blackbody radiation fields. *Planetary and Space Science*, *106*, 11–45. https://doi.org/10.1016/j.pss.2014.11.022

Itikawa, Y., & Mason, N. (2005). Cross sections for electron collisions with water molecules. *Journal of Physical and Chemical Reference Data*, *34*(1), 1–22. https://doi.org/10.1063/1.1799251

Johnson, R. E. (1990). *Energetic charged-particle interactions with atmospheres and surfaces*. Springer Science & Business Media.

Johnson, R. E., Carlson, R. W., Cooper, J. F., Paranicas, C., Moore, M. H., & Wong, M. C. (2004). Radiation effects on the surfaces of the Galilean satellites. *Jupiter: The Planet, Satellites and Magnetosphere*, *1*, 485–512.

Johnson, T. V. (1978). The Galilean satellites of Jupiter: Four worlds. *Annual Review of Earth and Planetary Sciences*, *6*(1), 93–125. https://doi.org/10.1146/annurev.ea.06.050178.000521

Kedzierski, W., Derbyshire, J., Malone, C., & McConkey, J. W. (1998). Isotope effects in the electron impact break-up of water. *Journal of Physics B: Atomic, Molecular and Optical Physics*, *31*(24), 5361. https://doi.org/10.1088/0953-4075/31/24/017

Killen, R., Shemansky, D., & Mouawad, N. (2009). Expected emission from Mercury's exospheric species, and their ultraviolet-visible signatures. *The Astrophysical Journal-Supplement Series*, *181*(2), 351–359. https://doi.org/10.1088/0067-0049/181/2/351

Kivelson, M. G., Bagenal, F., Kurth, W. S., Neubauer, F. M., Paranicas, C., & Saur, J. (2004). Magnetospheric interactions with satellites. *Jupiter: The Planet, Satellites and Magnetosphere*, *1*, 513–536.

Kliore, A. J., Anabtawi, A., Herrera, R. G., Asmar, S. W., Nagy, A. F., Hinson, D. P., & Flasar, F. M. (2002). Ionosphere of Callisto from Galileo radio occultation observations. *Journal of Geophysical Research*, *107*(A11), 1407. https://doi.org/10.1029/2002JA009365

Kollmann, P., Paranicas, C., Clark, G., Roussos, E., Lagg, A., & Krupp, N. (2016). The vertical thickness of Jupiter's Europa gas torus from charged particle measurements. *Geophysical Research Letters*, *43*, 9425–9433. https://doi.org/10.1002/2016GL070326

Krist, J. E., Hook, R. N., & Stoehr, F. (2011). 20 years of Hubble Space Telescope optical modeling using Tiny Tim. *Optical Modeling and Performance Predictions V*, *8127*, 81270J. https://doi.org/10.1117/12.892762

Kuskov, O. L., & Kronrod, V. A. (2005). Internal structure of Europa and Callisto. *Icarus*, *177*(2), 550–569. https://doi.org/10.1016/j.icarus.2005.04.014

Lagg, A., Krupp, N., & Williams, D. J. (2003). In-situ observations of a neutral gas torus at Europa. *Geophysical Research Letters*, *30*(11), 1556. https://doi.org/10.1029/2003GL017214

Leblanc, F., Oza, A. V., Leclercq, L., Schmidt, C., Cassidy, T., Modolo, R., et al. (2017). On the orbital variability of Ganymede's atmosphere. *Icarus*, *293*, 185–198. https://doi.org/10.1016/j.icarus.2017.04.025

Lewkow, N. R., & Kharchenko, V. (2014). Precipitation of energetic neutral atoms and induced non-thermal escape fluxes from the Martian atmosphere. *The Astrophysical Journal*, *790*(2), 98. https://doi.org/10.1088/0004-637x/790/2/98

Liang, M.-C., Lane, B. F., Pappalardo, R. T., Allen, M., & Yung, Y. L. (2005). Atmosphere of Callisto. *Journal of Geophysical Research*, *110*, E02003. https://doi.org/10.1029/2004JE002322

Liuzzo, L., Simon, S., Feyerabend, M., & Motschmann, U. (2016). Disentangling plasma interaction and induction signatures at Callisto: The Galileo C10 flyby. *Journal of Geophysical Research: Space Physics*, *121*, 8677–8694. https://doi.org/10.1002/2016JA023236

Liuzzo, L., Simon, S., & Regoli, L. (2019). Energetic electron dynamics near Callisto. *Planetary and Space Science*, *179*, 104726. https://doi.org/10.1016/j.pss.2019.104726

Mandeville, J.-C., Geake, J. E., & Dollfus, A. (1980). Reflectance polarimetry of Callisto and the evolution of the Galilean satellites. *Icarus*, *41*(3), 343–355. https://doi.org/10.1016/0019-1035(80)90219-5

Marconi, M. L. (2007). A kinetic model of Ganymede's atmosphere. *Icarus*, *190*, 155–174. https://doi.org/10.1016/j.icarus.2007.02.016

Mauk, B. H., Mitchell, D. G., Krimigis, S. M., Roelof, E. C., & Paranicas, C. P. (2003). Energetic neutral atoms from a trans-Europa gas torus at Jupiter. *Nature*, *421*(6926), 920–922. https://doi.org/10.1038/nature01431

McCord, T. B., Carlson, R. W., Smythe, W. D., Hansen, G. B., Clark, R. N., Hibbitts, C. A., et al. (1997). Organics and other molecules in the surfaces of Callisto and Ganymede. *Science*, *278*(5336), 271–275. https://doi.org/10.1126/science.278.5336.271

McCord, T. B., Hansen, G. B., Clark, R. N., Martin, P. D., Hibbitts, C. A., Fanale, F. P., et al. (1998). Non-water-ice constituents in the surface material of the icy Galilean satellites from the Galileo near-infrared mapping spectrometer investigation. *Journal of Geophysical Research*, *103*(E4), 8603–8626. https://doi.org/10.1029/98JE00788

Miller, R. H., & Combi, M. R. (1994). A Coulomb collision algorithm for weighted particle simulations. *Geophysical Research Letters*, *21*(16), 1735–1738. https://doi.org/10.1029/94GL01835

Moore, J. M., Asphaug, E., Morrison, D., Spencer, J. R., Chapman, C. R., Bierhaus, B., et al. (1999). Mass movement and landform degradation on the icy Galilean satellites: Results of the Galileo nominal mission. *Icarus*, *140*(2), 294–312. https://doi.org/10.1006/icar.1999.6132

Moore, J. M., Chapman, C. R., Bierhaus, E. B., Greeley, R., Chuang, F. C., Klemaszewskii, J., et al. (2004). Callisto. *Jupiter: The Planet, Satellites and Magnetosphere*, *1*, 397–426.

Morrison, D. (1977). Radiometry of satellites and of the rings of Saturn. *IAU Colloquium 28: Planetary Satellites* (p. 269).

Neubauer, F. M. (1998). The sub-Alfvénic interaction of the Galilean satellites with the Jovian magnetosphere. *Journal of Geophysical Research*, *103*(E9), 19843–19866. https://doi.org/10.1029/97JE03370

Oza, A. V., Leblanc, F., Johnson, R. E., Schmidt, C., Leclercq, L., Cassidy, T. A., & Chaufray, J.-Y. (2019). Dusk over dawn O_2 asymmetry in Europa's near-surface atmosphere. *Planetary and Space Science*, *167*, 23–32. https://doi.org/10.1016/j.pss.2019.01.006

Paranicas, C., Hibbitts, C. A., Kollmann, P., Ligier, N., Hendrix, A. R., Nordheim, T. A., et al. (2018). Magnetospheric considerations for solar system ice state. *Icarus*, *302*, 560–564. https://doi.org/10.1016/j.icarus.2017.12.013

Pilcher, C. B., Ridgway, S. T., & McCord, T. B. (1972). Galilean satellites: Identification of water frost. *Science*, *178*(4065), 1087–1089. https://doi.org/10.1126/science.178.4065.1087

Plainaki, C., Cassidy, T. A., Shematovich, V. I., Milillo, A., Wurz, P., Vorburger, A., et al. (2018). Towards a global unified model of Europa's tenuous atmosphere. *Space Science Reviews*, *214*(1), 40. https://doi.org/10.1007/s11214-018-0469-6

Purves, N. G., & Pilcher, C. B. (1980). Thermal migration of water on the Galilean satellites. *Icarus*, *43*(1), 51–55. https://doi.org/10.1016/0019-1035(80)90086-x

Rinaldi, G., Mura, A., Orsini, S., & Mangano, V. (2011). Report to cross sections related to plasma-planetary atmosphere interaction processes. *Planetary and Space Science*, *59*(9), 801–809. https://doi.org/10.1016/j.pss.2011.03.009

Roth, L., Alday, J., Becker, T. M., Ivchenko, N., & Retherford, K. D. (2017a). Detection of a hydrogen corona at Callisto. *Journal of Geophysical Research: Planets*, *122*, 1046–1055. https://doi.org/10.1002/2017JE005294

Roth, L., Ivchenko, N., Gladstone, G. R., Saur, J., Grodent, D., Bonfond, B., et al. (2021). A sublimated water atmosphere on Ganymede detected from Hubble Space Telescope observations. *Nature Astronomy*, *5*, 1043–1051. https://doi.org/10.1038/s41550-021-01426-9

Roth, L., Retherford, K. D., Ivchenko, N., Schlatter, N., Strobel, D. F., Becker, T. M., & Grava, C. (2017b). Detection of a hydrogen corona in HST Lyα images of Europa in transit of Jupiter. *The Astronomical Journal*, *153*(2), 67. https://doi.org/10.3847/1538-3881/153/2/67

Roth, L., Saur, J., Retherford, K. D., Feldman, P. D., & Strobel, D. F. (2014). A phenomenological model of Io's UV aurora based on HST/STIS observations. *Icarus*, *228*, 386–406. https://doi.org/10.1016/j.icarus.2013.10.009

Roush, T. L., Pollack, J. B., Witteborn, F. C., Bregman, J. D., & Simpson, J. P. (1990). Ice and minerals on Callisto: A reassessment of the reflectance spectra. *Icarus*, *86*(2), 355–382. https://doi.org/10.1016/0019-1035(90)90225-x

Sandford, S. A., & Allamandola, L. J. (1988). The condensation and vaporization behavior of H_2O: CO ices and implications for interstellar grains and cometary activity. *Icarus*, *76*(2), 201–224. https://doi.org/10.1016/0019-1035(88)90069-3

Sandford, S. A., & Allamandola, L. J. (1990). The volume- and surface-binding energies of ice systems containing CO, CO_2 and H_2O. *Icarus*, *87*(1), 188–192. https://doi.org/10.1016/0019-1035(90)90028-8

Sandford, S. A., & Allamandola, L. J. (1993). H_2 in interstellar and extragalactic ices-infrared characteristics, ultraviolet production, and implications. *The Astrophysical Journal*, *409*, L65–L68. https://doi.org/10.1086/186861

Scarlett, L. H., Tapley, J. K., Fursa, D. V., Zammit, M. C., Savage, J. S., & Bray, I. (2018). Electron-impact dissociation of molecular hydrogen into neutral fragments. *The European Physical Journal D*, *72*(2), 34. https://doi.org/10.1140/epjd/e2017-80649-8

Schmutz, W. K. (2021). Changes in the total solar irradiance and climatic effects. *Journal of Space Weather and Space Climate*, *11*, 40. https://doi.org/10.1051/swsc/2021016

Seufert, M. (2012). Callisto: Induction signals, atmosphere and plasma interaction (Doctoral dissertation). Retrieved from http://kups.ub.uni-koeln.de/4903

Sieveka, E. M., & Johnson, R. E. (1982). Thermal- and plasma-induced molecular redistribution on the icy satellites. *Icarus*, *51*(3), 528–548. https://doi.org/10.1016/0019-1035(82)90144-0

Smith, G. R., Shemansky, D. E., Broadfoot, A. L., & Wallace, L. (1978). Monte Carlo modeling of exospheric bodies: Mercury. *Journal of Geophysical Research*, *83*(A8), 3783–3790. https://doi.org/10.1029/JA083iA08p03783

Smith, H. T., Mitchell, D. G., Johnson, R. E., Mauk, B. H., & Smith, J. E. (2019). Europa neutral torus confirmation and characterization based on observations and modeling. *The Astrophysical Journal*, *871*(1), 69. https://doi.org/10.3847/1538-4357/aaed38

Smyth, W. H., & Marconi, M. L. (2006). Europa's atmosphere, gas tori, and magnetospheric implications. *Icarus*, *181*(2), 510–526. https://doi.org/10.1016/j.icarus.2005.10.019

Spencer, J. R. (1987a). Icy Galilean satellite reflectance spectra: Less ice on Ganymede and Callisto? *Icarus*, *70*(1), 99–110. https://doi.org/10.1016/0019-1035(87)90077-7

Spencer, J. R. (1987c). *The surface of Europa, Ganymede, and Callisto: An investigation using Voyager IRIS thermal infrared spectra (Doctoral dissertation)*. The University of Arizona. Retrieved from https://repository.arizona.edu/handle/10150/184058

Spencer, J. R. (1987b). Thermal segregation of water ice on the Galilean satellites. *Icarus*, *69*(2), 297–313. https://doi.org/10.1016/0019-1035(87)90107-2

Spencer, J. R., Lebofsky, L. A., & Sykes, M. V. (1989). Systematic biases in radiometric diameter determinations. *Icarus*, *78*(2), 337–354. https://doi.org/10.1016/0019-1035(89)90182-6

Spencer, J. R., & Maloney, P. R. (1984). Mobility of water ice on Callisto: Evidence and implications. *Geophysical Research Letters*, *11*(12), 1223–1226. https://doi.org/10.1029/GL011i012p01223

Spohn, T., & Schubert, G. (2003). Oceans in the icy Galilean satellites of Jupiter? *Icarus*, *161*(2), 456–467. https://doi.org/10.1016/s0019-1035(02)00048-9

Squyres, S. W. (1980). Surface temperatures and retention of H_2O frost on Ganymede and Callisto. *Icarus*, *44*(2), 502–510. https://doi.org/10.1016/0019-1035(80)90040-8

Squyres, S. W., & Veverka, J. (1981). Voyager photometry of surface features on Ganymede and Callisto. *Icarus*, *46*(2), 137–155. https://doi.org/10.1016/0019-1035(81)90203-7

Stewart, B. D., Pierazzo, E., Goldstein, D. B., Varghese, P. L., & Trafton, L. M. (2011). Simulations of a comet impact on the Moon and associated ice deposition in polar cold traps. *Icarus*, *215*(1), 1–16. https://doi.org/10.1016/j.icarus.2011.03.014

Straub, H. C., Renault, P., Lindsay, B. G., Smith, K. A., & Stebbings, R. F. (1996). Absolute partial cross sections for electron-impact ionization of H_2, N_2, and O_2 from threshold to 1000 eV. *Physical Review A*, *54*(3), 2146.

Strobel, D. F., Saur, J., Feldman, P. D., & McGrath, M. A. (2002). Hubble Space Telescope space telescope imaging spectrograph search for an atmosphere on Callisto: A Jovian unipolar inductor. *The Astrophysical Journal Letters*, *581*(1), L51–L54. https://doi.org/10.1086/345803

Szalay, J. R., Smith, H. T., Zirnstein, E. J., McComas, D. J., Begley, L. J., Bagenal, F., et al. (2022). Water-group pickup ions from Europa-genic neutrals orbiting Jupiter. *Geophysical Research Letters*, *49*, e2022GL098111. https://doi.org/10.1029/2022GL098111

Teolis, B. D., Plainaki, C., Cassidy, T. A., & Raut, U. (2017). Water ice radiolytic O_2, H_2, and H_2O_2 yields for any projectile species, energy, or temperature: A model for icy astrophysical bodies. *Journal of Geophysical Research: Planets*, *122*, 1996–2012. https://doi.org/10.1002/2017JE005285

Tseng, W.-L., Johnson, R. E., & Ip, W.-H. (2013). The atomic hydrogen cloud in the Saturnian system. *Planetary and Space Science*, *85*, 164–174. https://doi.org/10.1016/j.pss.2013.06.005

Tucker, O. J., Farrell, W. M., Killen, R. M., & Hurley, D. M. (2019). Solar wind implantation into the lunar regolith: Monte Carlo simulations of H retention in a surface with defects and the H_2 exosphere. *Journal of Geophysical Research: Planets*, *124*, 278–293. https://doi.org/10.1029/2018JE005805

Tucker, O. J., Farrell, W. M., & Poppe, A. R. (2021). On the effect of magnetospheric shielding on the lunar hydrogen cycle. *Journal of Geophysical Research: Planets*, *126*, e2020JE006552. https://doi.org/10.1029/2020JE006552

Turc, L., Leclercq, L., Leblanc, F., Modolo, R., & Chaufray, J.-Y. (2014). Modelling Ganymede's neutral environment: A 3D test-particle simulation. *Icarus*, *229*, 157–169. https://doi.org/10.1016/j.icarus.2013.11.005

Vorburger, A., Fatemi, S., Galli, A., Liuzzo, L., Poppe, A. R., & Wurz, P. (2021). 3D Monte-Carlo simulation of Ganymede's water exosphere. *Icarus*, *375*, 114810. https://doi.org/10.1016/j.icarus.2021.114810

Vorburger, A., Pfleger, M., Lindkvist, J., Holmström, M., Lammer, H., Lichtenegger, H. I. M., et al. (2019). 3D-modeling of Callisto's surface sputtered exosphere environment. *Journal of Geophysical Research: Space Physics*, *124*, 7157–7169. https://doi.org/10.1029/2019JA026610

Vorburger, A., Wurz, P., Lammer, H., Barabash, S., & Mousis, O. (2015). Monte-Carlo simulation of Callisto's exosphere. *Icarus*, *262*, 14–29. https://doi.org/10.1016/j.icarus.2015.07.035

Yung, Y. L., & McElroy, M. B. (1977). Stability of an oxygen atmosphere on Ganymede. *Icarus*, *30*(1), 97–103. https://doi.org/10.1016/0019-1035(77)90124-5